Automated procedure to derive convex failure envelope formulations for circular surface foundations under six degrees of freedom loading

Stephen K. Suryasentana[1], Harvey J. Burd[2], Byron W. Byrne[3], Avi Shonberg[4]

Affiliations

[1] Department of Civil and Environmental Engineering, University of Strathclyde, Glasgow, UK
(Orcid: 0000-0001-5460-5089)

[2] Department of Engineering Science, University of Oxford, Oxford, UK
(Orcid: 0000-0002-8328-0786)

[3] Department of Engineering Science, University of Oxford, Oxford, UK
(Orcid: 0000-0002-9704-0767)

[4] Ørsted Wind Power, London, UK

Corresponding author information

Stephen Suryasentana

stephen.suryasentana@strath.ac.uk

Abstract

Failure envelope formulations are typically employed to assess the ultimate capacity of foundations under combined loading and for incorporation in macro-element models. However, the complex interaction between each load component, especially for six degree of freedom (6DoF) loading, means that determining satisfactory formulations is often a complex process. Previous researchers have identified this difficulty as an obstacle to the adoption of the failure envelope approach in foundation engineering applications. To address this issue, the paper describes a systematic procedure for deriving globally convex failure envelope formulations; the procedure is applied to a circular surface foundation, bearing on undrained clay, in 6DoF load space. The formulations are shown to closely represent the failure load combinations determined from finite element analyses for a variety of loading conditions, including non-planar horizontal-moment loading. An example macro-element model based on the proposed formulation is described; the macro-element model provides a close representation of the foundation behaviour determined from a separate finite element analysis. A key aspect of the paper is that it demonstrates an automated process to determine well-behaved failure envelope formulations. The automated nature of the process has considerable advantages over the manual procedures that have previously been employed to determine failure envelope formulations.

Keywords

Bearing capacity, Failure, Foundations, Soil-structure interaction, Offshore engineering, Numerical modelling

List of notation

V	vertical load
H_x	horizontal load along x-axis
H_y	horizontal load along y-axis
M_x	moment about x-axis
M_y	moment about y-axis
Q	torque about z-axis
V_0	vertical uniaxial capacity
H_0	horizontal uniaxial capacity
M_0	moment uniaxial capacity
Q_0	torsion uniaxial capacity
$\tilde{V}$	normalised vertical load
$\tilde{H}_x$	normalised horizontal load along x-axis
$\tilde{H}_y$	normalised horizontal load along y-axis
$\tilde{M}_x$	normalised moment about x-axis
$\tilde{M}_y$	normalised moment about y-axis
$\tilde{Q}$	normalised torque about z-axis
H_i	horizontal load along a general axis i in the x-y plane
M_i	moment about a general axis i in x-y plane
$\tilde{H}_i$	normalised horizontal load along a general axis i in x-y plane
$\tilde{M}_i$	normalised moment about a general axis i in x-y plane
s_{u}	undrained shear strength

Highlights

- Previous failure envelope formulations were typically determined using a manual process that may be very time-consuming, especially for a high-dimensional load space.
- The paper describes an automated procedure to determine failure envelope formulations for a circular surface foundation in the full six degrees of freedom load space.
- Advantages of the derived failure envelope formulations, compared with previous formulations, include guaranteed global convexity (which allows the formulation to be used for both ultimate capacity evaluation and macro-element modelling), thermodynamic consistency (if used as a plastic potential) and accurate modelling of the failure envelope for non-planar horizontal-moment loading.
- Advantages of the proposed procedure includes fast computational time, minimal manual interpretation of failure data, and generality of the procedure for other circular foundation configurations (e.g. suction caisson or bucket foundations).

1. Introduction

1.1 Failure envelope approach in foundation design

A failure envelope is a hypersurface that defines combinations of loads and moments that result in the ultimate limit state of a foundation. The failure envelope approach is widely used to assess the ultimate capacity of shallow foundations for combined loading, as recommended by several design guidelines (e.g. Paikowsky, 2010; API, 2011; ISO, 2016). Failure envelopes are typically represented by a closed-form mathematical formulation (referred to in this paper as a 'failure envelope formulation'). Several failure envelope formulations have been derived by previous researchers by fitting selected parametric functions to failure load data obtained from numerical analysis and/or experiments. Unlike traditional bearing capacity analysis, the failure envelope approach is able to explicitly model complex interactions for combined loading, rather than using simple linear superposition methods incorporating load inclination and eccentricity.

However, deriving satisfactory failure envelope formulations for specific foundation engineering applications is typically a challenging task, especially for six degree of freedom (6DoF) loading conditions, due to the complex interactions between the load components. Thus, the process of deriving these formulations tends to be difficult and time-consuming, as even the first step of identifying a suitable functional form for the formulation may not be straightforward. For drained loading, effective – and relatively simple - 6DoF failure envelope formulations have been previously developed for foundations on sand (e.g. Bienen et al. 2006; Salciarini & Tamagnini 2009); these formulations provide a good fit with experimental data. However, for undrained loading, the shapes of the failure envelope, e.g. derived from numerical analysis, are typically rather more complex and deriving a failure envelope formulation that fits the data well in these cases is challenging. Previous researchers (e.g. Gourvenec, 2007; Shen et al., 2017) have identified practical difficulties in deriving suitable formulations as a notable obstacle to increased adoption of the failure envelope approach in practical applications.

In addition to the various practical difficulties in deriving satisfactory failure envelope formulations in 6DoF load space, many of the existing failure envelope formulations are not

numerically convenient for use as yield surfaces of macro-element models due to their functional forms. Furthermore, most previous failure envelope formulations adopt idealised ground conditions such as uniform or linearly increasing undrained shear strength s_u with depth (for clay) or uniform friction angle (for sand); these conditions may not be realistic for sites with more complex (e.g. multi-layered) ground conditions. There is therefore a need for a systematic procedure to facilitate the formulation of numerically well-conditioned failure envelopes for site-specific conditions; the current paper presents a process that is suitable for this purpose.

1.2 Previous failure envelope formulations for surface footings on undrained clay

The current paper is concerned with failure envelope formulations for a rigid circular surface foundation on undrained clay. Various failure envelope formulations for this foundation configuration are proposed in the literature (e.g. Taiebat & Carter, 2000; Gourvenec & Randolph, 2003; Gourvenec, 2007; Vulpe et al., 2014; Shen et al., 2017). These previous formulations typically represent undrained clay using the Tresca or von Mises yield criteria. In the following discussion, clay modelled using the Tresca and von Mises yield criteria are referred to as 'Tresca soil' and 'von Mises soil' respectively.

In the following discussion, the nomenclature $\tilde{V}, \tilde{H}, \tilde{M}\ \tilde{Q}$ is used to indicate normalised values of vertical force, V, horizontal force, H, moment M and torque Q applied to the foundation such that $\tilde{V} = V/V_0$, $\tilde{H} = H/H_0$, $\tilde{M} = M/M_0$ and $\tilde{Q} = Q/Q_0$ where V_0, H_0, M_0, Q_0 are the respective uniaxial capacities (i.e. the ultimate capacities of the foundation due to each individual load or moment/torque component). For 6DoF loading, $\tilde{H}_x, \tilde{M}_y, \tilde{H}_y, \tilde{M}_x$ refers to the normalised values of the horizontal force (along x-axis), moment (about y-axis), horizontal force (along y-axis) and moment (about x-axis) respectively i.e. $\tilde{H}_x = H_x/H_0$, $\tilde{M}_y = M_y/M_0$, $\tilde{H}_y = H_y/H_0$, $\tilde{M}_x = M_x/M_0$. The conventions employed in this paper to define the 6DoF loads (consistent with Butterfield et al. 1997) applied to a circular surface foundation are depicted in Fig. 1.

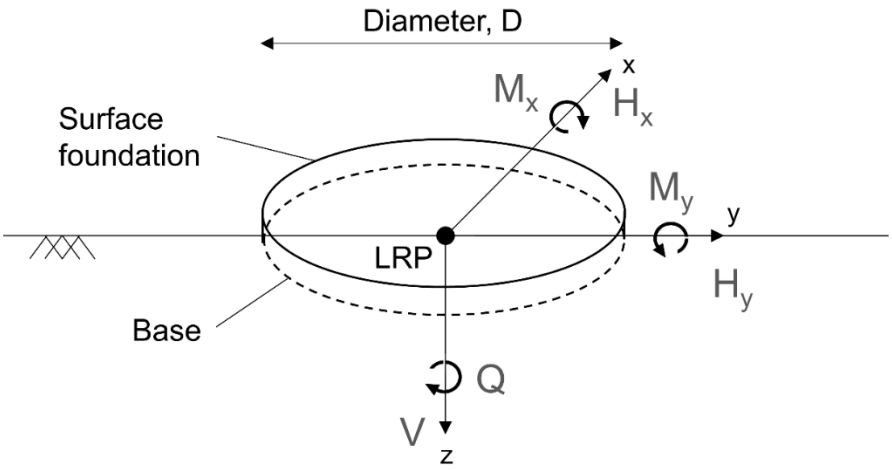

147
148 **Figure 1.** 6DoF loading configuration for surface foundation, consistent with the conventions in
149 Butterfield et al. (1997). The loading reference point (LRP) is at the centre of the foundation
150 base.
151

152 The difficulty in deriving failure envelope formulations increases with increased dimension of the
153 load space; as a consequence there are few previous formulations that account for the
154 complete 6DoF load space (i.e. comprising loads and moments in each of the three coordinate
155 directions). Most previous failure envelope formulations are limited to three load components
156 V, H and M applied to the foundation, where H is the resultant horizontal force considered to be
157 planar with the resultant moment M, as defined in Butterfield et al. (1997). This limited VHM
158 load space may not be adequate for modelling foundations that support offshore structures such
159 as offshore wind turbines, where the wind and wave actions may result in H that is non-planar
160 with M. Nevertheless, such formulations are useful for design scenarios where the limited load
161 space provides a realistic representation of the main load drivers on the foundation.
162

163 For circular surface foundations on Tresca soil (for uniform undrained shear strength and no
164 contact breaking between soil and foundation), Taiebat & Carter (2000) and Vulpe et al. (2014)
165 proposed two different VHM failure envelope formulations. Taiebat & Carter (2000) proposed
166 the formulation,

$$f(\tilde{H},\tilde{M},\tilde{V}) = |\tilde{H}^3| + \left(\tilde{M}\left(1 - 0.3\tilde{H}\frac{\tilde{M}}{|\tilde{M}|}\right)\right)^2 - \tilde{V}^2 - 1 = 0 \quad (1)$$

167 Vulpe et al. (2014) proposed the alternative formulation,

$$f(\tilde{H},\tilde{M},\tilde{V}) = \left|\frac{\tilde{H}}{\xi_{\mathrm{H}}}\right|^{a} + \left(\frac{\tilde{M}}{\xi_{\mathrm{M}}}\right)^{a} + 2b\left(\frac{\tilde{H}\tilde{M}}{\xi_{\mathrm{H}}\xi_{\mathrm{M}}}\right) - 1 = 0 \quad (2)$$

where

$$\xi_{\mathrm{H}} = 1 - \tilde{V}^{4.69}$$

$$\xi_{\mathrm{M}} = 1 - \tilde{V}^{2.12}$$

$$a = 2.13 \text{ if } \tilde{V} \leq 0.5 \text{ else } a = 1.63$$

$$b = -0.26 \text{ if } \tilde{V} \leq 0.5 \text{ else } b = -0.05$$

Alternative values of a and b for Tresca soil with linearly increasing undrained shear strength with depth are provided in Vulpe et al. (2014).

One of the few previous failure envelope formulations for circular surface foundations for the complete 6DoF load space is described in Shen et al. (2017). This failure envelope formulation, which relates to foundations on Tresca soil (for both uniform and linearly increasing strength with depth and no contact breaking between soil and foundation) is defined by,

$$f(\tilde{H},\tilde{M},\tilde{V},\tilde{Q}) = \left(\frac{\tilde{H}}{\xi_{\mathrm{H}}}\right)^{2} + \left(\frac{\tilde{M}}{\xi_{\mathrm{M}}}\right)^{a}\left(1 - b\frac{\tilde{H}}{\xi_{\mathrm{H}}}\right) - 1 = 0 \quad (3)$$

where the normalised resultant horizontal force $\tilde{H}$ and normalised resultant moment $\tilde{M}$ are not necessarily planar. The coefficients in Eq. 3 are given by,

$$a = 2.1 + 0.2\left(1 + \frac{\tilde{H}}{|\tilde{H}|}\right) - \left(1.1 - 0.1\left(1 + \frac{\tilde{H}}{|\tilde{H}|}\right)\right)\tilde{V} + \left(2.4 - 1.8\left(1 + \frac{\tilde{H}}{|\tilde{H}|}\right)\right)\tilde{V}^{2}$$

$$b = 0.5 + 0.1\left(1 + \frac{\tilde{H}}{|\tilde{H}|}\right) - 0.1\tilde{V} - 0.6\tilde{V}^{2}$$

$$\xi_{\mathrm{H}} = \xi_{\mathrm{H0}}\left(1 - \left(\frac{\tilde{Q}}{\xi_{\mathrm{Q}}}\right)^{1.75}\right)^{0.571}$$

$$\xi_{\mathrm{M}} = \left(1 - \tilde{V}^{\frac{1}{0.28+0.035\kappa-0.002\kappa^{2}}}\right)\left(1 - \left(\frac{\tilde{Q}}{\xi_{\mathrm{Q}}}\right)^{1.5+0.1\tilde{V}+1.4\tilde{V}^{2}}\right)^{\frac{1}{(5.3+\tilde{V}-6\tilde{V}^{2})(1+(0.09-0.02\tilde{V}-0.15\tilde{V}^{2})\kappa)}}$$

$$\xi_{\mathrm{H0}} = 1 \text{ if } \tilde{V} \leq 0.5 \text{ else } \left(1 - \left(2\tilde{V} - 1\right)^{2}\right)^{0.667}$$

$$\xi_{\mathrm{Q}} = 1 \text{ if } \tilde{V} \leq 0.5 \text{ else } \left(1 - \left(2\tilde{V} - 1\right)^{4}\right)^{0.4}$$

where κ is the gradient of the linearly increasing soil strength profile.

Shen et al. (2017) found that the influence of the resultant horizontal force H and moment M on the failure envelope depends on the relative directions in which H and M are applied. In particular, the failure characteristics change when H and M depart from being planar. Note that Eq. 3 does not attempt to accurately represent the failure envelope under non-planar HM loading. Instead, it represents a conservative, lower bound failure envelope for all possible H and M directions. Eqs. 2 and 3 have similar functional forms; both are derived using a procedure referred to in this paper as the 'HM-based' procedure. In this approach, the formulation is initially defined in the HM load space. The influence of additional load components (e.g. V or Q) are then incorporated within the formulation by reducing the uniaxial capacities (i.e. H_0 or M_0) using 'knock-down' factors (ξ_{H} or ξ_{M}) that represent the reduction of capacities due to interactions with vertical force and/or torsion.

Looking beyond circular surface foundations (the particular focus of the current paper), 6DoF failure envelope formulations have been previously developed for other foundation types. For example, Martin (1994) proposed the following formulation for spudcan foundations,

$$f(\tilde{H}_x, \tilde{M}_y, \tilde{H}_y, \tilde{M}_x, \tilde{V}, \tilde{Q}) = \left(\tilde{H}_x{}^2 + \tilde{H}_y{}^2\right) + \left(\tilde{M}_x{}^2 + \tilde{M}_y{}^2\right) - 2a\left(\tilde{H}_y\tilde{M}_x - \tilde{H}_x\tilde{M}_y\right) + \tilde{Q}^2 - b\tilde{V}^{2\beta_1}(1-\tilde{V})^{2\beta_2} = 0 \quad (4)$$

where a, b, β_1, β_2 are fitting parameters. Eq. 4 was later adopted by Bienen et al. (2006) and Salciarini & Tamagnini (2009) for the yield surfaces of their macro-element models for circular surface foundations on sand. One of the main limitations of Eq. 4 is that it is only able to represent a limited range of failure envelope shapes, for example it does not provide a good fit with failure data of surface foundations on undrained clay, especially in the HM load space (where Eq. 4 models an elliptical-shaped failure envelope contour). It also suffers from numerical issues such as singularities at some load values such as $\tilde{V} = 1$, where difficulties arise in calculating the gradient. For mudmat foundations, Feng et al. (2014a, 2014b, 2015a, 2015b) proposed 6DoF failure envelope formulations, similar in form to Eq. 3.

There are various limitations in previous failure envelope formulations for circular surface foundations on undrained clay. First, there are no validated failure envelope formulations that accurately represent the failure envelope for cases where H and M are non-planar. Second,

most of the existing failure envelope formulations are unsatisfactory for use as a yield surface or plastic potential in macro-element models, as they may not be real-valued for parts of the load space and numerical issues exist (e.g. singularities at some load values); this makes numerical implementation inconvenient. It is noted that singularities, e.g. at $\tilde{V} = 1$, may be genuine features of the failure behaviour, but it is typically desirable - for numerical robustness – to approximate these singularities by employing smooth functions. Third, previous formulations are not always guaranteed to be thermodynamically consistent, if used as plastic potentials in macro-element models. Previous formulations are also typically not globally convex, therefore they may cause numerical issues when using implicit elasto-plastic integration algorithms (Panteghini & Lagioia, 2014, 2018a, 2018b). Finally, the HM-based procedure is currently the most common framework for deriving failure envelope formulations for 6DoF loading and this has been successfully applied to mudmat foundations (e.g. Feng et al., 2014a, 2014b, 2015a, 2015b) and surface foundations (Shen et al., 2017). This procedure, however, may not produce failure envelope formulations that are suitable for macro-element modelling and significant manual interpretation is required to formulate the knockdown factors (ξ_{H} or ξ_{M}) for each additional load component (V or Q). Therefore, an automated procedure that can derive the complete failure envelope formulation with minimal manual interpretation would be advantageous.

1.3 Objectives of the current paper

The current paper aims to address the practical difficulties – referred to in the previous section - in deriving failure envelope formulations for 6DoF loading; an automated process is proposed, based on sum of squares convex (SOS-convex) polynomials, employing the framework described in Suryasentana et al. (2020a). This framework guarantees a failure envelope formulation that is globally convex (which facilitates the use of efficient implicit elastic-plastic integration algorithms in macro-element models) and thermodynamically consistent (if used as a plastic potential in a macro-element model). Moreover, the formulation is numerically 'well-behaved' (i.e. no singularities in the load space and gradients can be easily calculated), which further enhances its suitability for use in macro-element modelling.

The paper extends the work of Suryasentana et al. (2020a) by demonstrating how *a priori* knowledge of the invariance of the failure envelope with respect to horizontal and moment loading (due to the circular geometry of the foundation) can be incorporated within the framework to guarantee that the derived formulation satisfies this invariant property. The proposed automated process is, in principle, applicable to any foundation with circular symmetry (e.g. suction caisson or bucket foundations) and in any laterally homogeneous ground conditions (i.e. no spatial variations in the horizontal plane) – including nonhomogeneous depth-wise soil strength variation. The current paper, however, considers the 6DoF failure envelope formulation for a circular surface foundation on undrained homogeneous clay as an example application. The failure envelope formulation is calibrated using failure load data generated by 3D finite element calibration analyses.

2. Method

2.1 Load conventions

Planar HM loading corresponds to the case where $H = H_y$ and $M = M_x$. A failure envelope formulation f for the 6DoF load space is defined as,

$$f(H_x, M_y, H_y, M_x, V, Q) = 0 \tag{5}$$

Furthermore, H_i is defined as the resultant horizontal load along axis i and M_j is the resultant moment about axis j; these axes can be aligned in arbitrary directions in the x-y plane. Due to the circular geometry of the problem, the failure envelope is governed by the relative directions of H_i and M_j, and not their absolute directions. In other words, the failure envelope is invariant to changes in the absolute directions of H_i and M_j, provided that their relative directions remain the same. This invariant property can be represented by a failure envelope formulation for a reduced five degrees of freedom (5DoF) load space of the form:

$$f(\alpha, H_i, M_j, V, Q) = 0 \tag{6}$$

where α is a parameter that represents the relative direction of H_i with respect to M_j.

The parameter α is represented by $\alpha_{HM'}$, which is the absolute (unsigned) angle between H_i and $M_j{}'$, where the $M_j{}'$ direction is clockwise orthogonal to the M_j direction (see Fig. 2). It is

emphasised that $\alpha_{HM'}$ is not defined as the angle between H_i and M_j, as this definition cannot differentiate between $\pm H_i$ or $\pm M_j$ for planar HM loading. For planar HM loading, the absolute angle between H_i and M_j is always $\pi/2$ radians, regardless of whether H_i and M_j are positive or negative valued; this would imply that the HM failure envelope should be identical in all quadrants of the HM load space, which would contradict previous research. On the other hand, for planar HM loading, the absolute angle between H_i and ${M_j}'$ (or $-H_i$ and $-{M_j}'$) is zero, while the absolute angle between $-H_i$ and ${M_j}'$ (or H_i and $-{M_j}'$) is π radians. The definition adopted for $\alpha_{HM'}$ can distinguish the correct symmetry of these various loading scenarios. Conveniently, in the current convention $\alpha_{HM'} = 0$ represents the planar HM loading case.

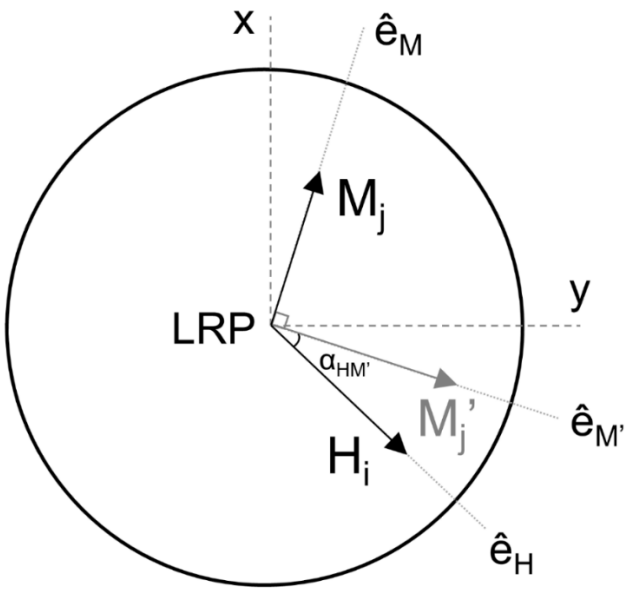

Figure 2. Conventions adopted for general $\boldsymbol{H}$-$\boldsymbol{M}$ loading, where the loading reference point (LRP) is at the centre of the foundation base.

2.2 Finite element model

To calibrate the failure envelope formulation, failure load calibration data were generated for multiple combinations of $\alpha_{HM'}, H_i, M_j, V, Q$. Data were generated until it was concluded that a sufficient number had been obtained to define a smooth failure surface, e.g. by visual inspection of *HM* contours of the failure envelope for different combinations of $\alpha_{HM'}, H_i, M_j, V, Q$ throughout their valid ranges. The calibration data were generated by conducting three-dimensional (3D)

finite element analyses of a rigid circular surface foundation of diameter D on homogeneous undrained clay using the finite element software Abaqus v6.13 (Dassault Systèmes 2014). The diameter and depth of the finite element mesh domain were set to $6D$ and $2.5D$ respectively. This domain size was found to be sufficiently large to avoid significant boundary effects on the computed failure loads, as the maximum change in the uniaxial capacities of the foundation was 0.3% when the domain was doubled (i.e. diameter of $12D$ and depth of $5D$). Furthermore, Shen et al. (2017) used a similar-sized mesh domain (diameter of 6D and depth of 3D), which they found to be sufficiently large for the failure mechanisms to be unaffected by the mesh boundaries. Displacements were fixed in all directions at the bottom of the mesh and in the radial directions on its periphery. A representative mesh is shown in Fig. 3.

The soil was defined as a homogeneous, isotropic linear elastic, perfectly plastic material, with undrained shear strength s_{u}, adopting a fully-associated von Mises yield criterion. This von Mises model was selected for the current study, rather than a Tresca model, as the built-in Tresca model implemented in Abaqus does not employ a fully-associated flow rule (instead, the von Mises function is adopted as the plastic potential). Since the macro-element model example described later in this paper adopts an associated flow rule, it is considered important that the Abaqus analyses also adopt a fully-associated soil constitutive model. This facilitates a fair comparison of the load-displacement calculations conducted with the macro-element model and the Abaqus finite element analysis.

The Poisson's ratio ν of the soil was set to 0.49, while its Young's modulus E was set to $1000\sqrt{3}s_{\mathrm{u}}$. (The Young's modulus may be set arbitrarily since the elastic behaviour does not affect the final failure states, Chen & Liu 1990). First-order, fully-integrated, linear, brick elements C3D8H were adopted for the soil. The surface foundation was modelled as a weightless, rigid body, and the loading reference point was set at the centre of its base, as shown in Fig. 1. Separation and slip at the soil-foundation interface was prevented using tie constraints.

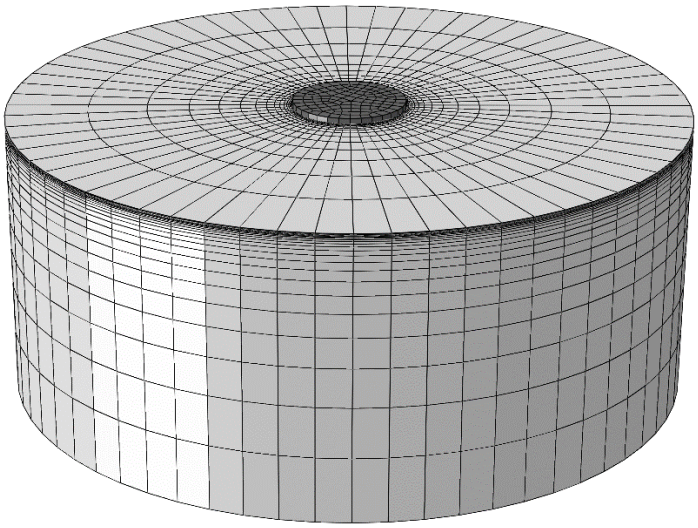

(a)

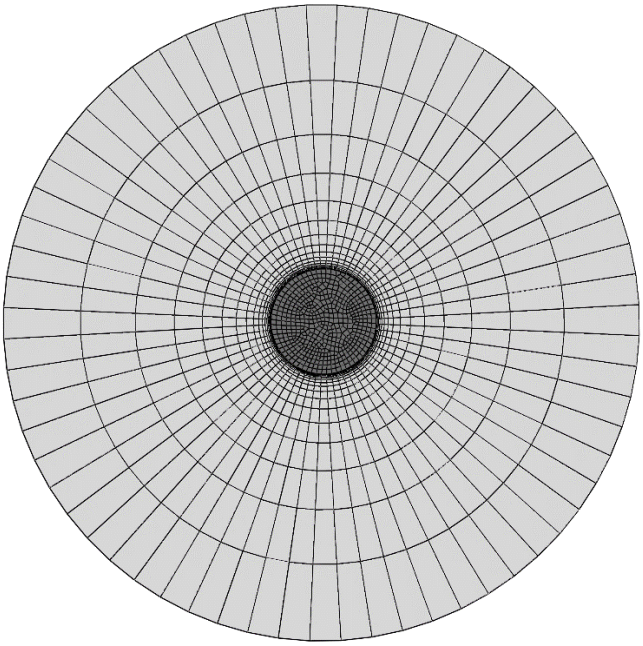

(b)

Figure 3. (a) Oblique view of the 3D finite element model. The diameter and depth of the mesh domain are $\boldsymbol{6D}$ and $\boldsymbol{2.5D}$ respectively. (b) Plan view of the 3D finite element model.

2.3 Numerical procedures to determine failure load data

First, the uniaxial load capacities (Q_0, V_0, H_0, M_0) of the foundation were computed by independently prescribing displacements of $0.1D$ and rotations of 0.1 radians in the respective axes; these displacement/rotation magnitudes were sufficiently large to reach failure (i.e. the load had reached steady state).

Next, failure load data were determined to map the reduced load space ($\alpha_{HM'}, H_i, M_j, V, Q$) using combined displacement and load controls. The $QVHM$ failure envelope was explored by finding HM contours of the failure envelope using displacement control, after applying fixed levels of Q and V using load control. Specifically, Q and/or V loads were first applied on the foundation, before horizontal displacements and rotations were applied onto the foundation using the 'sequential swipe' test described in Suryasentana et al. 2020c; this analysis procedure facilitates an efficient and robust process for mapping the failure envelope. The sequential swipe test is a modification of the single swipe test introduced by Tan (1990), which is a displacement-controlled procedure that has been widely employed to obtain failure load data to construct failure envelopes for shallow foundations. A single swipe test consists of two sequential steps in which a displacement is applied on the foundation in one degree of freedom (DoF) until the failure load is reached, followed by the application of a displacement on the foundation in another DoF while the displacement in the first DoF is held constant. The sequential swipe test essentially breaks down the second step into multiple steps, to smoothen the transition between one DoF to another. In the current paper, the 16-swipe sequential swipe test was implemented in the HM load space; '16-swipe' here means that the second step of the single swipe test is subdivided into 16 smaller steps (further details are provided in Suryasentana et al. 2020c).

To conduct the sequential swipe test for non-planar HM loading, a specified torque and vertical load is first applied to the foundation; values of normalised torque and vertical load adopted in the current work were $\tilde{Q} = 0, 0.25, 0.5, 0.75$ and $\tilde{V} = 0, 0.25, 0.5, 0.75$. Thereafter, a rotation Θ_x is applied about the *x*-axis, as shown in Fig. 4, until failure is reached. Increasing increments of horizontal displacement S_H is then applied together with decreasing increments of Θ_x (in 16 steps) at specified values of $\alpha_{S\Theta}$, where $\alpha_{S\Theta}$ is the angle between the direction of S_H and the normal to Θ_x, as indicated in Fig. 4. The loci of points on the failure surface are computed during this 16-steps phase. Three values of $\alpha_{S\Theta} = 0, \pi/4, \pi/2$ were adopted to map the failure surface.

The computed horizontal force H is not necessarily co-directional with S_H (except for the special cases of $\alpha_{S\Theta} = 0, \pi/2$). In general, the angle $\alpha_{HM'}$ (which defines the angular separation between the horizontal force and moment directions) takes different values from $\alpha_{S\Theta}$ (which

defines the angular separation between the displacement and rotation directions. This feature of the analysis has certain implications for mapping the failure surface since (except for $\alpha_{S\Theta} = \alpha_{HM'} = 0, \pi/2$) it is not possible to specify, precisely, the values of $\alpha_{HM'}$ at which the failure envelope is sampled. Instead, values of $\alpha_{S\Theta}$ are selected that are judged to provide appropriate coverage of the failure surface; the current choice of $\alpha_{S\Theta} = 0, \pi/4, \pi/2$ was found to work well. For $\alpha_{S\Theta} = \pi/4$, the value of $\alpha_{HM'}$ was found to diverge from $\alpha_{S\Theta}$ by an amount that depended on the current values of H and M, although the angle remained in the range $0 \leq \alpha_{HM'} \leq \pi/2$.

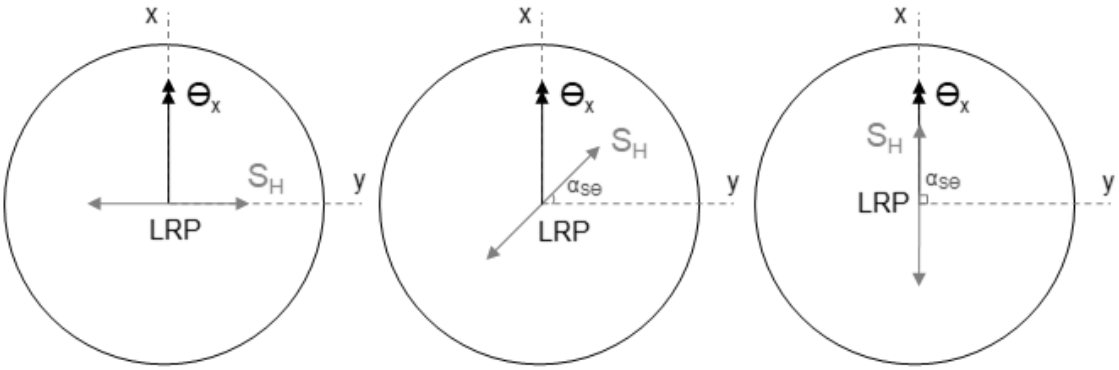

Figure 4. Displacement boundary conditions applied for non-planar HM loading.

Table 1 provides comparisons between the 3D finite element uniaxial load capacity results from this study, the analytical solution from Finnie & Morgan (2004) and 3D finite element limit analysis (FELA) results from Suryasentana et al. (2020c). The 3D finite element results generally agree well with these previous solutions; this comparison provides evidence of the reliability of the current numerical procedures.

Table 1. Uniaxial capacities of the surface foundation, where $A = \pi D^2/4$ refers to the foundation base area.

	$\frac{Q_0}{ADs_u}$	$\frac{V_0}{As_u}$	$\frac{H_0}{As_u}$	$\frac{M_0}{ADs_u}$
3D finite element	0.344	5.63	1.02	0.714
3D FELA (LB)	-	5.45	1.00	0.667
3D FELA (UB)	-	5.77	1.00	0.715
3D FELA (Average)	-	5.61	1.00	0.691
Analytical	0.333	-	-	-

2.4 SOS-convex polynomial failure envelope framework

A failure envelope formulation – employing SOS-convex polynomials as the basis functions – is employed to provide a fit with the failure load data computed by 3D finite element analysis. This SOS-convex polynomial framework – which is described in detail in Suryasentana et al. (2020a) - has the advantageous characteristic that failure envelope formulations are generated that are guaranteed to be globally convex and numerically well-behaved. Moreover, the framework has been previously shown to be able to fit failure load data for a range of cases, albeit in the planar VHM load space.

The formulation in Suryasentana et al. (2020a) is concerned only with 3DoF loading (in planar VHM load space). The current paper extends this previous work by deriving failure envelope formulations in the full 6DoF load space. The SOS-convex polynomial failure envelope framework employed in the current work is reviewed briefly below. Further details are provided in Suryasentana et al. (2020a).

2.4.1. SOS-convex polynomials

A sum of squares (SOS) polynomial $s(\boldsymbol{x})$ of degree 2*d* (*d* is a positive integer) is defined as,

$$s(\boldsymbol{x}) = \sum_{j=1}^{npoly} g_j(\boldsymbol{x})^2 \tag{7}$$

where $g_j(\boldsymbol{x})$ are polynomials of degree $\leq d$, *npoly* is the number of individual polynomials and $\boldsymbol{x}$ is a vector containing individual coordinates.

A convex polynomial $h(\boldsymbol{x})$ is a polynomial with a Hessian $\nabla^2 h(\boldsymbol{x})$ that satisfies the condition,

$$\boldsymbol{y}^{\mathrm{T}} \nabla^2 h(\boldsymbol{x}) \boldsymbol{y} \geq 0 \text{ for all } \boldsymbol{x}, \boldsymbol{y} \in \text{domain of } h \tag{8}$$

where $\boldsymbol{y}$ is a vector. An SOS-convex polynomial $p(\boldsymbol{x})$ is a polynomial with a Hessian $\nabla^2 p(\boldsymbol{x})$ that satisfies the condition,

$$\boldsymbol{y}^{\mathrm{T}} \nabla^2 p(\boldsymbol{x}) \boldsymbol{y} \text{ is SOS for all } \boldsymbol{x}, \boldsymbol{y} \in \text{domain of } p \tag{9}$$

Since a sum of squares is always non-negative, an SOS-convex polynomial also satisfies Eq. 8 and is thus a convex polynomial too. SOS-convex polynomials are adopted as the basis

functions for the failure envelope formulations, as the requirement in Eq. 9 is computationally more tractable than Eq. 8 and can readily be incorporated within the search process for failure envelope formulations using semidefinite programming (Parrilo 2003).

2.4.2 Procedure for formulating the failure envelope

A failure envelope formulation is sought, of the form in Eq. 6, that provides a good fit with the 3D finite element calibration data. On the basis of the procedures outlined in Suryasentana et al. (2020a), a homogeneous SOS-convex polynomial $p\left(\alpha_{HM'}, H_i, M_j, V, Q\right)$ is sought to represent the failure envelope formulation f in the form,

$$f\left(\alpha_{HM'}, H_i, M_j, V, Q\right) = p\left(\alpha_{HM'}, H_i, M_j, V, Q\right) - 1 \tag{10}$$

The current work necessitates the development of new procedures - not considered in Suryasentana et al. (2020a) - to include the effect of $\alpha_{HM'}$ (which needs to be treated differently from H_i, M_j, V, Q to ensure that the derived failure envelope formulation is physically sensible).

The first step is to choose the degree of the homogeneous polynomial basis functions, where a homogeneous polynomial is defined as a polynomial whose non-zero terms all have the same degree. The framework requires the selection of 'even degree' polynomials. It is desirable to select the lowest polynomial degree that achieves an acceptable fit with failure envelope data, since lower degree polynomials are more compact, containing fewer terms. A 2nd degree homogeneous polynomial is the most compact form, but its data-fitting capabilities are limited as it can only model ellipsoidal surfaces. The 4th degree homogeneous polynomial is typically the most compact polynomial form that allows a reasonable fit to be achieved with typical failure envelope shapes. Higher degree polynomials may provide a better fit with data, as they have more parameters, but this is at the expense of increased complexity in the formulation. For the current study, 4th and 6th degree homogeneous polynomial basis functions were chosen. These choices facilitate an investigation on whether 4th degree polynomial basis functions provide an acceptable level of fidelity and whether significant improvements can be achieved by employing higher degree (6th degree) polynomials.

As an illustrative example, let $p_0(H_i, M_j)$ be a 4th degree homogeneous polynomial in just the H_i and M_j components,

$$p_0(H_i, M_j) = H_i^4 a_1 + H_i^3 M_j a_2 + H_i^2 M_j^2 a_3 + H_i M_j^3 a_4 + M_j^4 a_5 \tag{11}$$

where a_i are coefficients that will be determined to best fit the failure load data (under the constraint that the polynomial is SOS-convex). Next, special treatment is required to include the effect of $\alpha_{HM'}$ within $p_0(H_i, M_j)$. It is known from physical intuition that if the horizontal loading is applied along the moment axis (i.e. $\alpha_{HM'} = \pi/2$), the failure envelope response should be symmetric in all quadrants of the HM load space. Effectively, this means that all the HM coupling terms in the failure envelope should reduce to zero when $\alpha_{HM'} = \pi/2$, as these terms govern the asymmetry in the HM load space. This can be achieved by replacing all HM coupling terms with $HM\cos\alpha_{HM'}$ coupling terms. For example, Eq. 11 can be replaced by,

$$\begin{aligned} p_1(\alpha_{HM'}, H_i, M_j) = {} & H_i^4 a_1 + H_i^2 (H_i M_j \cos\alpha_{HM'}) a_2 + (H_i M_j \cos\alpha_{HM'})^2 a_3 \\ & + M_j^2 (H_i M_j \cos\alpha_{HM'}) a_4 + M_j^4 a_5 \end{aligned} \tag{12}$$

Using Eq. 12, $p_1(\alpha_{HM'} = \pi/2, H_i, M_j) = H_i^4 a_1 + M_j^4 a_5$, which is symmetric in all quadrants of the HM load space. Therefore, the complete 4th degree or 6th degree homogeneous polynomials for the full load space (i.e. $p(\alpha_{HM'}, H_i, M_j, V, Q)$ in Eq. 10) can be obtained by first generating the homogeneous polynomial in a reduced $\{H_i, M_j, V, Q\}$ load space and then replacing all HM coupling terms with $HM\cos\alpha_{HM'}$ coupling terms.

After the functional form of $p(\alpha_{HM'}, H_i, M_j, V, Q)$ has been finalised, the coefficients are determined using the failure load data from the 3D finite element calibration analyses. A single finite element analysis provides a single set of failure load data in the 6DoF load space i.e. $\{H_x, M_y, H_y, M_x, V, Q\}$. These data need to be transformed to the reduced load space of $\{\alpha_{HM'}, H_i, M_j, V, Q\}$. This is achieved by letting the axis i point along the resultant horizontal load vector $\boldsymbol{H}_i$ and the axis j point along the resultant moment vector $\boldsymbol{M}_j$. Moreover, let $\boldsymbol{M}_j'$ be the moment vector that is clockwise orthogonal to $\boldsymbol{M}_j$ i.e.,

$$\boldsymbol{H}_i = \begin{bmatrix} H_x \\ H_y \end{bmatrix} \quad (13)$$
$$\boldsymbol{M}_j = \begin{bmatrix} M_x \\ M_y \end{bmatrix}$$
$$\boldsymbol{M}_j{}' = \begin{bmatrix} -M_y \\ M_x \end{bmatrix}$$

460 H_i and M_j are then defined as the magnitude of $\boldsymbol{H}_i$ and $\boldsymbol{M}_j$ respectively i.e.,

$$H_i = |\boldsymbol{H}_i| = \sqrt{H_x^2 + H_y^2} \quad (14)$$

$$M_j = |\boldsymbol{M}_j| = \sqrt{M_x^2 + M_y^2}. \quad (15)$$

461 and $\alpha_{HM'}$ can be calculated using the dot product rule as,

$$\alpha_{HM'} = \cos^{-1}\left(\frac{\boldsymbol{H}_i \cdot \boldsymbol{M}_j{}'}{H_i M_j}\right). \quad (16)$$

462 Thereafter, the transformed failure load data are standardised by normalising each load
463 component by its respective uniaxial capacity. For example, the transformed failure loads from a
464 single finite element analysis $\{\alpha_{HM'}, H_i, M_j, V, Q\}$ is standardised to $\{\alpha_{HM'}, H_i/H_0, M_j/M_0, V/V_0, Q/$
465 $Q_0\}$ or equivalently $\{\alpha_{HM'}, \tilde{H}_i, \tilde{M}_j, \tilde{V}, \tilde{Q}\}$.

466

467 The final step is to use the standardised failure load data to determine the SOS-convex
468 polynomial coefficients in $p(\alpha_{HM'}, H_i, M_j, V, Q)$. Some of the coefficients can be identified
469 straightforwardly using the uniaxial loading conditions and other symmetry principles (see
470 Suryasentana et al. 2020a). The remaining coefficients are determined by convex optimisation.
471 This is achieved by solving the following convex optimisation problem, which is based on the
472 conditions: (i) p is SOS-convex and (ii) p provides a best fit with the failure load calibration data
473 in a 'least-squares' sense:

$$\text{minimize} \quad \sum_{i=1}^{ndata} \left(p(\bar{\boldsymbol{x}}_i^{\boldsymbol{data}}) - 1\right)^2 \quad (17)$$

$$\text{subject to} \quad p \text{ is SOS-convex (i.e. } p \text{ satisfies Eq. 9)}$$

474 where $\bar{\boldsymbol{x}}_i^{\boldsymbol{data}} = \{\alpha_{HM'}, \tilde{H}_i, \tilde{M}_j, \tilde{V}, \tilde{Q}\}$ is a set of failure load data determined from the finite element
475 analyses and *ndata* is the total number of failure load data sets. The MATLAB toolbox 'YALMIP'
476 (Löfberg, 2004, 2009), which is a free-to-use and specialised toolbox for solving SOS problems,
477 was employed to set up the functional forms of the homogeneous polynomials p and
478 automatically solve Eq. 17 to determine the coefficients in p.

3. Results

3.1 Failure envelope formulations

3.1.1 Formulations in reduced space

Table 2 lists the objective values (and their corresponding root-mean values) for both failure envelope formulations (based on 4th and 6th degree polynomials) at the end of the optimisation defined in Eq. 17. It can be observed that p_6 (6th degree polynomial) has a slightly better fit to the calibration data than p_4 (4th degree polynomial), as it has a lower objective value.

Table 2. Minimised objective values $C = \sum_{i=1}^{ndata}\left(p\left(\bar{\boldsymbol{x}}_{\boldsymbol{i}}^{\boldsymbol{data}}\right) - 1\right)^2$ in Eq. 17 for p_4 and p_6 at the end of the optimisation process using the 3D finite element failure load data. $ndata = 1950$ is the total number of failure load data sets. The last two columns in the table provide the root-mean-square (RMS) errors for the failure envelope formulations.

	C for p_4	C for p_6	$\sqrt{\frac{C}{ndata}}$ for p_4	$\sqrt{\frac{C}{ndata}}$ for p_6
Minimised values	114.46	86.26	0.242	0.21

On the basis of Eq. 10, the 4th degree failure envelope formulation is $f_4 = p_4 - 1$; this may be expressed as,

$$f_4\left(\alpha_{HM'}, \tilde{H}_i, \tilde{M}_j, \tilde{V}, \tilde{Q}\right) = \tilde{H}_i^{\,4} + \tilde{M}_j^{\,4} + \tilde{V}^4 + \tilde{Q}^4 - 1 + I_{HM} + I_{VH} + I_{VM} + I_{QH} + I_{QM} + I_{VHM} + I_{QHM} \tag{18}$$

where the I terms represent interactions between different load components, as indicated in the subscripts. For example, I_{HM} represents the interaction between horizontal and moment loading, while I_{VHM} represents the interaction between vertical, horizontal and moment loading. These interaction terms incorporate the values of the coefficients determined from the optimisation in Eq. 17 and they are defined in Table 3.

Similarly, the 6th degree failure envelope formulation, $f_6 = p_6 - 1$, is expressed as,

$$f_6(\alpha_{HM'}, \tilde{H}_i, \tilde{M}_j, \tilde{V}, \tilde{Q}) = \tilde{H_i}^6 + \tilde{M_j}^6 + \tilde{V}^6 + \tilde{Q}^6 - 1 + I_{HM} + I_{VH} + I_{VM} + I_{QH} + I_{QM} + I_{VHM} + I_{QHM} + I_{QV} + I_{QVH} + I_{QVM} + I_{QVHM} \quad (19)$$

where the interaction terms are also defined in Table 3.

Table 3. Definitions of the interaction terms for the 4th degree failure envelope formulation f_4 and 6th degree failure envelope formulation f_6, as determined by the optimisation process in Eq 17. The load components involved in each interaction term are shown in the subscript e.g. I_{HM} represents the interaction between H and M.

Interaction term	f_4	f_6
I_{HM}	$-0.36\tilde{H_i}^2(\tilde{H_i}\tilde{M_j}\cos\alpha_{HM'}) + 0.9(\tilde{H_i}\tilde{M_j}\cos\alpha_{HM'})^2 - 1.43\tilde{M_j}^2(\tilde{H_i}\tilde{M_j}\cos\alpha_{HM'})$	$-0.33\tilde{H_i}^4(\tilde{H_i}\tilde{M_j}\cos\alpha_{HM'}) + 1.22\tilde{H_i}^2(\tilde{H_i}\tilde{M_j}\cos\alpha_{HM'})^2 - 2.17(\tilde{H_i}\tilde{M_j}\cos\alpha_{HM'})^3 + 2.34\tilde{M_j}^2(\tilde{H_i}\tilde{M_j}\cos\alpha_{HM'})^2$
I_{VH}	$0.4\tilde{H_i}^2\tilde{V}^2$	$1.97\tilde{H_i}^2\tilde{V}^4 + 0.03\tilde{H_i}^4\tilde{V}^2$
I_{VM}	$1.64\tilde{M_j}^2\tilde{V}^2$	$0.84\tilde{M_j}^4\tilde{V}^2 + 4.72\tilde{M_j}^2\tilde{V}^4$
I_{QH}	$2.61\tilde{H_i}^2\tilde{Q}^2$	$4.56\tilde{H_i}^4\tilde{Q}^2 + 3.47\tilde{H_i}^2\tilde{Q}^4$
I_{QM}	$0.34\tilde{M_j}^2\tilde{Q}^2$	$1.65\tilde{M_j}^4\tilde{Q}^2 + 0.16\tilde{M_j}^2\tilde{Q}^4$
I_{VHM}	$0.84\tilde{V}^2(\tilde{H_i}\tilde{M_j}\cos\alpha_{HM'})$	$0.34\tilde{H_i}^2\tilde{V}^2(\tilde{H_i}\tilde{M_j}\cos\alpha_{HM'}) + 0.29\tilde{M_j}^2\tilde{V}^2(\tilde{H_i}\tilde{M_j}\cos\alpha_{HM'}) + 1.52\tilde{V}^4(\tilde{H_i}\tilde{M_j}\cos\alpha_{HM'}) + 1.1\tilde{H_i}^2\tilde{M_j}^2\tilde{V}^2$
I_{QHM}	$-0.84\tilde{Q}^2(\tilde{H_i}\tilde{M_j}\cos\alpha_{HM'})$	$-1.92\tilde{H_i}^2\tilde{Q}^2(\tilde{H_i}\tilde{M_j}\cos\alpha_{HM'}) - 4.53\tilde{M_j}^2\tilde{Q}^2(\tilde{H_i}\tilde{M_j}\cos\alpha_{HM'}) - 0.58\tilde{Q}^4(\tilde{H_i}\tilde{M_j}\cos\alpha_{HM'}) + 4.62\tilde{H_i}^2\tilde{M_j}^2\tilde{Q}^2$
I_{QV}	-	$0.55\tilde{V}^4\tilde{Q}^2 + 0.12\tilde{V}^2\tilde{Q}^4$
I_{QVH}	-	$0.46\tilde{H_i}^2\tilde{V}^2\tilde{Q}^2$
I_{QVM}	-	$0.67\tilde{M_j}^2\tilde{V}^2\tilde{Q}^2$
I_{QVHM}	-	$1.75\tilde{V}^2\tilde{Q}^2(\tilde{H_i}\tilde{M_j}\cos\alpha_{HM'})$

517 *3.1.2 Transformation to 6DoF load space*

518 For implementation purposes (e.g. for the macro-element example described in Section 5), it is

519 convenient to redefine Eqs. 18 and 19 in terms of $\widetilde{H}_x, \widetilde{M}_y, \widetilde{H}_y, \widetilde{M}_x$, as that would avoid the need

520 to calculate $\alpha_{HM'}, \widetilde{H}_i, \widetilde{M}_j$. This is achieved by noting that the dot product of $\boldsymbol{H}_i$ and $\boldsymbol{M}_j{}'$ is

521 equivalent to,

$$\begin{aligned} \boldsymbol{H}_i \cdot \boldsymbol{M}_j{}' &= \begin{bmatrix} H_x \\ H_y \end{bmatrix} \cdot \begin{bmatrix} -M_y \\ M_x \end{bmatrix} \\ &= H_y M_x - H_x M_y \end{aligned} \tag{20}$$

522 The dot product of $\boldsymbol{H}_i$ and $\boldsymbol{M}_j{}'$ can also be represented in terms of $\alpha_{HM'}$ as,

$$\boldsymbol{H}_i \cdot \boldsymbol{M}_j{}' = H_i M_j \cos \alpha_{HM'} \tag{21}$$

523 Using Eqs. 20 and 21, the term $\widetilde{H}_i \widetilde{M}_j \cos \alpha_{HM'}$ in Eqs. 18 and 19 can be expanded to,

$$\begin{aligned} \widetilde{H}_i \widetilde{M}_j \cos \alpha_{HM'} &= \frac{H_i M_j \cos \alpha_{HM'}}{H_0 M_0} \\ &= \frac{H_y M_x - H_x M_y}{H_0 M_0} \\ &= \widetilde{H}_y \widetilde{M}_x - \widetilde{H}_x \widetilde{M}_y \end{aligned} \tag{22}$$

524 Using Eqs. 14, 15 and 22, Eq. 17 is redefined as,

$$\begin{aligned} f_4\left(\widetilde{H}_x, \widetilde{M}_y, \widetilde{H}_y, \widetilde{M}_x, \tilde{V}, \tilde{Q}\right) = &\left(\widetilde{H}_x{}^2 + \widetilde{H}_y{}^2\right)^2 + \left(\widetilde{M}_x{}^2 + \widetilde{M}_y{}^2\right)^2 + \tilde{V}^4 + \tilde{Q}^4 - 1 \\ &+ I_{HM} + I_{VH} + I_{VM} + I_{QH} + I_{QM} \\ &+ I_{VHM} + I_{QHM} \end{aligned} \tag{23}$$

525 where the interaction terms are defined in Table 4. Similarly, Eq. 18 is redefined as,

$$\begin{aligned} f_6\left(\widetilde{H}_x, \widetilde{M}_y, \widetilde{H}_y, \widetilde{M}_x, \tilde{V}, \tilde{Q}\right) = &\left(\widetilde{H}_x{}^2 + \widetilde{H}_y{}^2\right)^3 + \left(\widetilde{M}_x{}^2 + \widetilde{M}_y{}^2\right)^3 + \tilde{V}^6 + \tilde{Q}^6 - 1 \\ &+ I_{HM} + I_{VH} + I_{VM} + I_{QH} + I_{QM} \\ &+ I_{VHM} + I_{QHM} \\ &+ I_{QV} + I_{QVH} + I_{QVM} + I_{QVHM} \end{aligned} \tag{24}$$

where the interaction terms are also defined in Table 4.

Table 4. Redefinitions of the interaction terms shown in Table 3, in terms of $\tilde{H}_x, \tilde{M}_y, \tilde{H}_y, \tilde{M}_x$.

Interaction term	f_4	f_6
I_{HM}	$-0.36\left(\tilde{H}_x{}^2+\tilde{H}_y{}^2\right)\left(\tilde{H}_y\tilde{M}_x-\tilde{H}_x\tilde{M}_y\right)$ $+0.9\left(\tilde{H}_y\tilde{M}_x-\tilde{H}_x\tilde{M}_y\right)^2$ $-1.43\left(\tilde{M}_x{}^2+\tilde{M}_y{}^2\right)\left(\tilde{H}_y\tilde{M}_x-\tilde{H}_x\tilde{M}_y\right)$	$-0.33\left(\tilde{H}_x{}^2+\tilde{H}_y{}^2\right)^2\left(\tilde{H}_y\tilde{M}_x-\tilde{H}_x\tilde{M}_y\right)$ $+1.22\left(\tilde{H}_x{}^2+\tilde{H}_y{}^2\right)\left(\tilde{H}_y\tilde{M}_x-\tilde{H}_x\tilde{M}_y\right)^2$ $-2.17\left(\tilde{H}_y\tilde{M}_x-\tilde{H}_x\tilde{M}_y\right)^3$ $+2.34\left(\tilde{M}_x{}^2+\tilde{M}_y{}^2\right)\left(\tilde{H}_y\tilde{M}_x-\tilde{H}_x\tilde{M}_y\right)^2$
I_{VH}	$0.4\left(\tilde{H}_x{}^2+\tilde{H}_y{}^2\right)\tilde{V}^2$	$1.97\left(\tilde{H}_x{}^2+\tilde{H}_y{}^2\right)\tilde{V}^4$ $+0.03\left(\tilde{H}_x{}^2+\tilde{H}_y{}^2\right)^2\tilde{V}^2$
I_{VM}	$1.64\left(\tilde{M}_x{}^2+\tilde{M}_y{}^2\right)\tilde{V}^2$	$0.84\left(\tilde{M}_x{}^2+\tilde{M}_y{}^2\right)^2\tilde{V}^2$ $+4.72\left(\tilde{M}_x{}^2+\tilde{M}_y{}^2\right)\tilde{V}^4$
I_{QH}	$2.61\left(\tilde{H}_x{}^2+\tilde{H}_y{}^2\right)\tilde{Q}^2$	$4.56\left(\tilde{H}_x{}^2+\tilde{H}_y{}^2\right)^2\tilde{Q}^2$ $+3.47\left(\tilde{H}_x{}^2+\tilde{H}_y{}^2\right)\tilde{Q}^4$
I_{QM}	$0.34\left(\tilde{M}_x{}^2+\tilde{M}_y{}^2\right)\tilde{Q}^2$	$1.65\left(\tilde{M}_x{}^2+\tilde{M}_y{}^2\right)^2\tilde{Q}^2$ $+0.16\left(\tilde{M}_x{}^2+\tilde{M}_y{}^2\right)\tilde{Q}^4$
I_{VHM}	$0.84\tilde{V}^2\left(\tilde{H}_y\tilde{M}_x-\tilde{H}_x\tilde{M}_y\right)$	$0.34\left(\tilde{H}_x{}^2+\tilde{H}_y{}^2\right)\tilde{V}^2\left(\tilde{H}_y\tilde{M}_x-\tilde{H}_x\tilde{M}_y\right)$ $+0.29\left(\tilde{M}_x{}^2+\tilde{M}_y{}^2\right)\tilde{V}^2\left(\tilde{H}_y\tilde{M}_x-\tilde{H}_x\tilde{M}_y\right)$ $+1.52\tilde{V}^4\left(\tilde{H}_y\tilde{M}_x-\tilde{H}_x\tilde{M}_y\right)$ $+1.1\left(\tilde{H}_x{}^2+\tilde{H}_y{}^2\right)\tilde{M}_j{}^2\tilde{V}^2$
I_{QHM}	$-0.84\tilde{Q}^2\left(\tilde{H}_y\tilde{M}_x-\tilde{H}_x\tilde{M}_y\right)$	$-1.92\left(\tilde{H}_x{}^2+\tilde{H}_y{}^2\right)\tilde{Q}^2\left(\tilde{H}_y\tilde{M}_x-\tilde{H}_x\tilde{M}_y\right)$ $-4.53\left(\tilde{M}_x{}^2+\tilde{M}_y{}^2\right)\tilde{Q}^2\left(\tilde{H}_y\tilde{M}_x-\tilde{H}_x\tilde{M}_y\right)$ $-0.58\tilde{Q}^4\left(\tilde{H}_y\tilde{M}_x-\tilde{H}_x\tilde{M}_y\right)$ $+4.62\left(\tilde{H}_x{}^2+\tilde{H}_y{}^2\right)\left(\tilde{M}_x{}^2+\tilde{M}_y{}^2\right)\tilde{Q}^2$
I_{QV}	-	$0.55\tilde{V}^4\tilde{Q}^2+0.12\tilde{V}^2\tilde{Q}^4$
I_{QVH}	-	$0.46\left(\tilde{H}_x{}^2+\tilde{H}_y{}^2\right)\tilde{V}^2\tilde{Q}^2$
I_{QVM}	-	$0.67\left(\tilde{M}_x{}^2+\tilde{M}_y{}^2\right)\tilde{V}^2\tilde{Q}^2$
I_{QVHM}	-	$1.75\tilde{V}^2\tilde{Q}^2\left(\tilde{H}_y\tilde{M}_x-\tilde{H}_x\tilde{M}_y\right)$

3.2 Coupling between failure load components

Certain aspects of the coupling between individual failure load components are discussed below in connection with projections of the failure envelope onto the HM plane (i.e. HM contours).

3.2.1 Influence of $\tilde{V}$ on the failure envelope

Fig. 5 shows the HM failure envelope contours for different values of $\tilde{V}$, for $\alpha_{HM'} = 0$ (i.e. planar HM loading) and $\tilde{Q} = 0$. It is evident that for increased $\tilde{V}$, the available HM capacity decreases. The reduction in HM capacity is relatively small for $\tilde{V} \leq 0.5$, but it increases in significance for $\tilde{V} > 0.5$. Furthermore, the asymmetry in the HM load space becomes negligible at high $\tilde{V}$ loading (e.g. $\tilde{V} = 0.75$); this indicates that the vertical load has a significant influence on the interaction between $\tilde{H}$ and $\tilde{M}$.

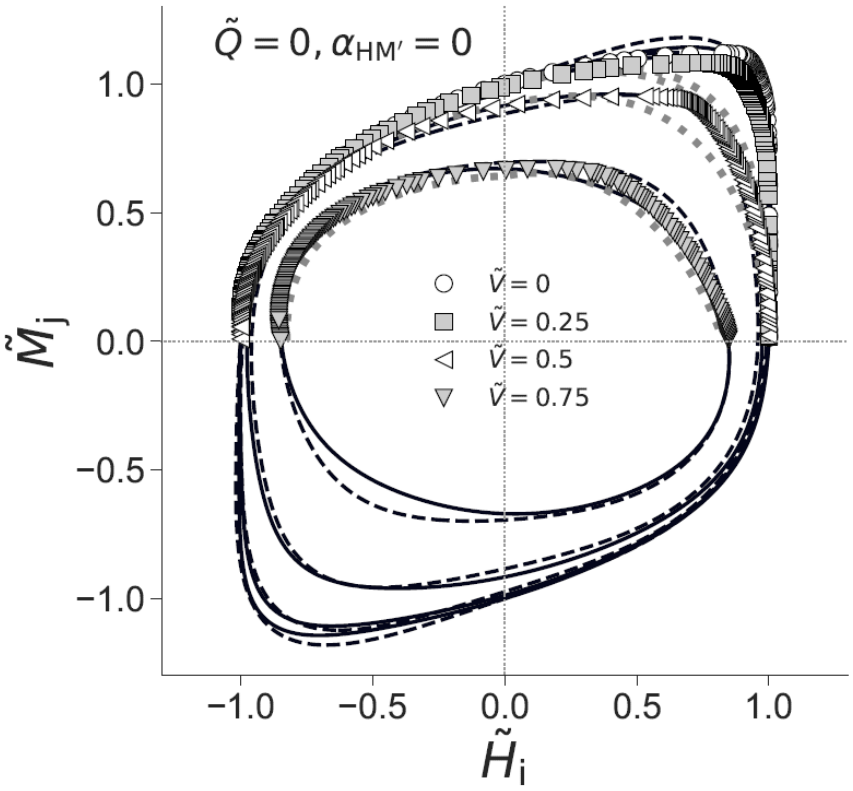

Figure 5. $\boldsymbol{HM}$ failure envelope contours for $\boldsymbol{\alpha_{HM'} = 0, \tilde{V} = 0, 0.25, 0.5, 0.75}$ and $\boldsymbol{\tilde{Q} = 0}$. The black dashed and solid lines are the contours represented by $\boldsymbol{f_4}$ and $\boldsymbol{f_6}$ respectively. The grey dotted lines are the contours represented by the Shen et al. (2017) formulation (Eq. 3).

3.2.2 Influence of $\tilde{\boldsymbol{Q}}$ on the failure envelope

Fig. 6 shows the effect of normalised torque $\tilde{Q}$ on the HM failure envelope contours for different values of $\tilde{Q}$, for $\alpha_{HM'} = 0$. As $\tilde{Q}$ loading increases, the available HM capacity is seen to decrease. However, unlike the influence of the vertical loading, the application of a torque appears to have minimal influence on the general shape of the HM contours.

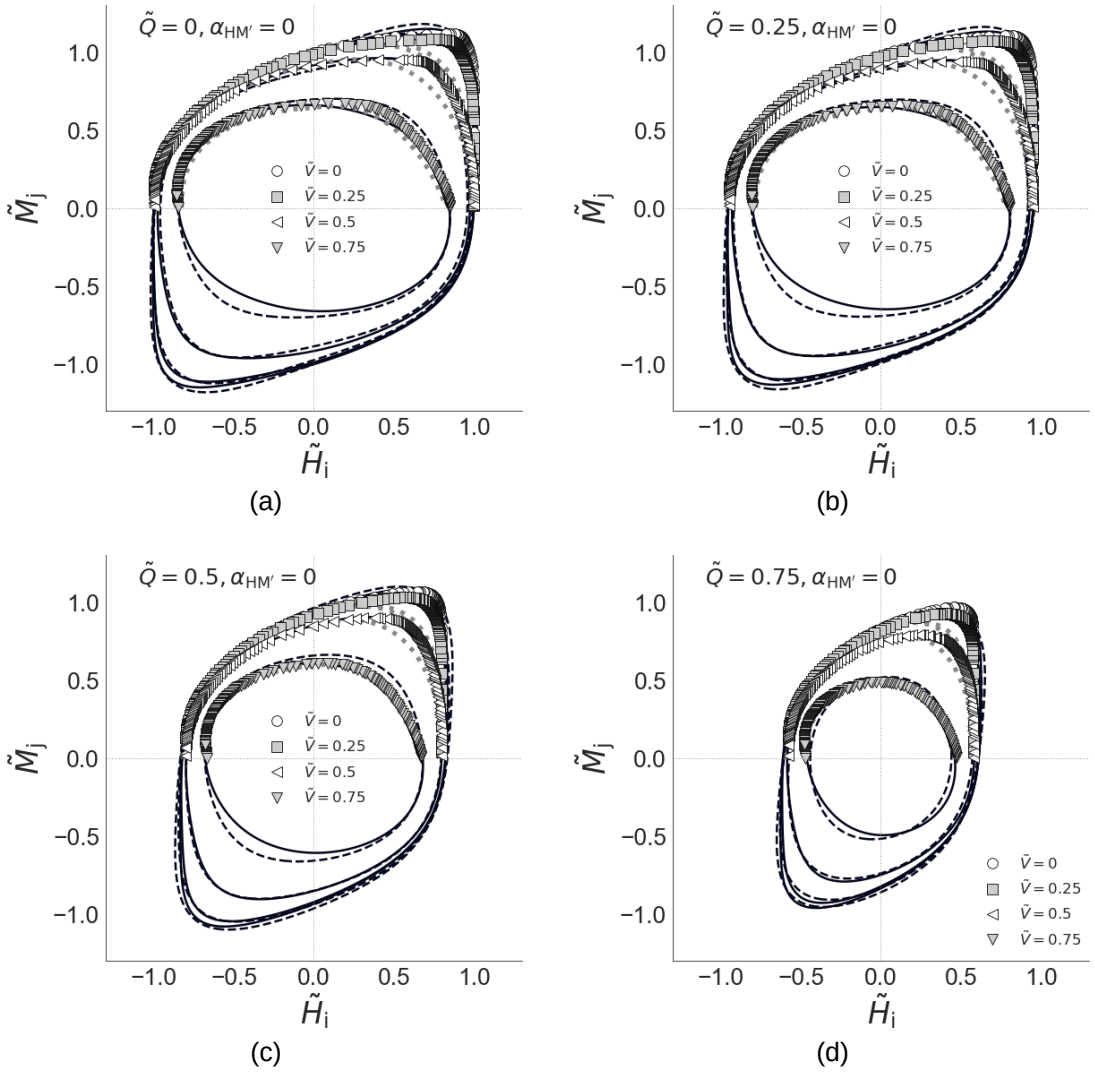

Figure 6. $\boldsymbol{HM}$ failure envelope contours for $\boldsymbol{\alpha_{HM'} = 0, \tilde{V} = 0, 0.25, 0.5, 0.75}$ and (a) $\boldsymbol{\tilde{Q} = 0}$; (b) $\boldsymbol{\tilde{Q} = 0.25}$; (c) $\boldsymbol{\tilde{Q} = 0.5}$; (d) $\boldsymbol{\tilde{Q} = 0.75}$. The black dashed and solid lines are the contours represented by $\boldsymbol{f_4}$ and $\boldsymbol{f_6}$ respectively. The grey dotted lines are the contours represented by the Shen et al. (2017) formulation (Eq. 3).

3.2.3 Effect of $\boldsymbol{\alpha_{HM'}}$ on the failure envelope

Fig. 7 shows the effect of non-planar HM loading (through $\alpha_{HM'}$) on the HM contours of the failure envelope for different values of $\tilde{V}$, for $Q = 0$. Only the results for $0 \leq \alpha_{HM'} \leq \pi/2$ are shown in the figure, as the results for $\pi/2 < \alpha_{HM'} \leq \pi$ are the mirror image about the M_j axis (i.e. reflection about the $H_i = 0$ line) of the results for $\pi - \alpha_{HM'}$. For example, the results for $\alpha_{HM'} = \pi$ is the mirror image of the results for $\alpha_{HM'} = 0$. There are fewer failure load data points in Fig. 7b,c as the resultant H from $\alpha_{S\Theta} = \pi/4$ corresponds to a range of $\alpha_{HM'}$ (recall that $\alpha_{HM'} \neq \alpha_{S\Theta}$). The asymmetry in the HM load space decreases as $\alpha_{HM'}$ increases from 0, until there is no asymmetry at $\alpha_{HM'} = \pi/2$. Fig. 8 shows the effects of $\alpha_{HM'}$ and combined V and Q loading on the HM contours; these effects are consistent with the observed trends in Figs. 5-7.

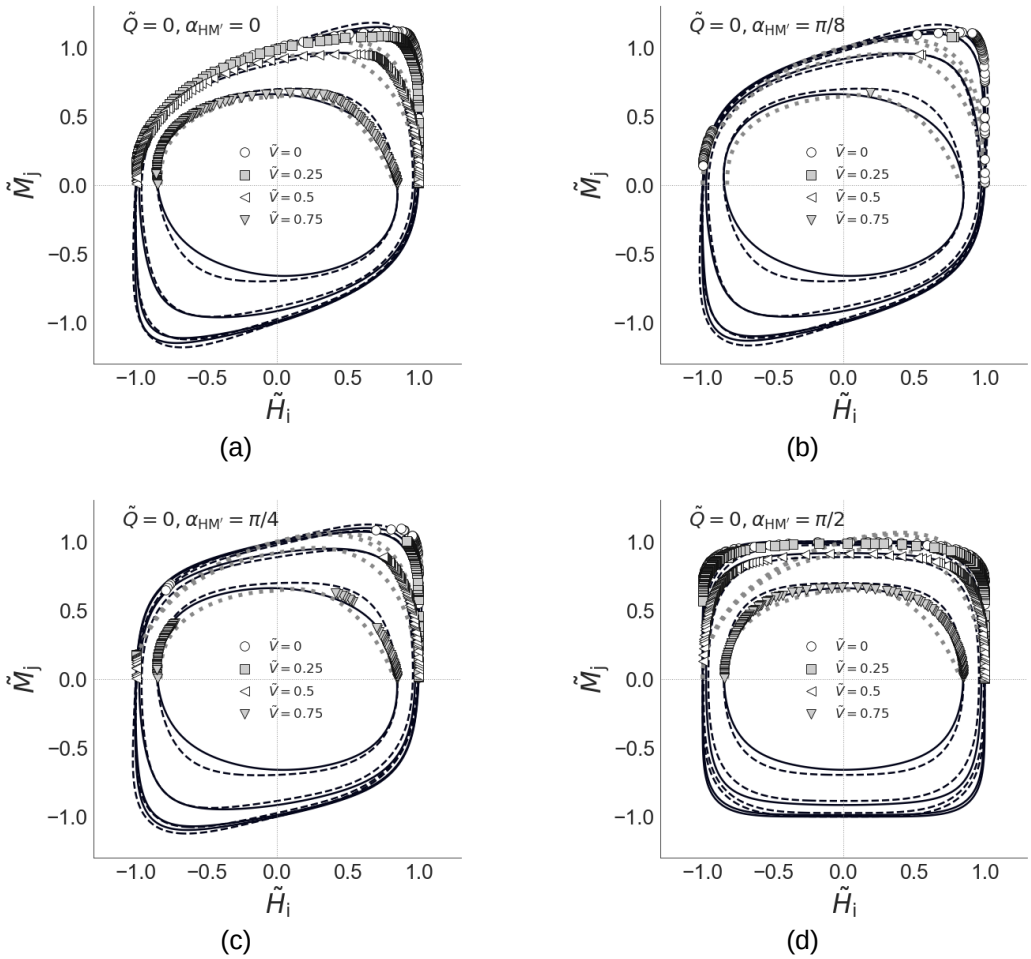

Figure 7. $\boldsymbol{HM}$ failure envelope contours for $\widetilde{\boldsymbol{Q}} = \mathbf{0}$, $\widetilde{\boldsymbol{V}} = \mathbf{0}, \mathbf{0.25}, \mathbf{0.5}, \mathbf{0.75}$, and (a) $\boldsymbol{\alpha_{HM'}} = \mathbf{0}$; (b) $\boldsymbol{\alpha_{HM'}} = \frac{\boldsymbol{\pi}}{\mathbf{8}}$; (c) $\boldsymbol{\alpha_{HM'}} = \frac{\boldsymbol{\pi}}{\mathbf{4}}$; (d) $\boldsymbol{\alpha_{HM'}} = \frac{\boldsymbol{\pi}}{\mathbf{2}}$. The black dashed and solid lines are the contours represented by $\boldsymbol{f_4}$ and $\boldsymbol{f_6}$ respectively. The grey dotted lines are the contours represented by the Shen et al. (2017) formulation (Eq. 3).

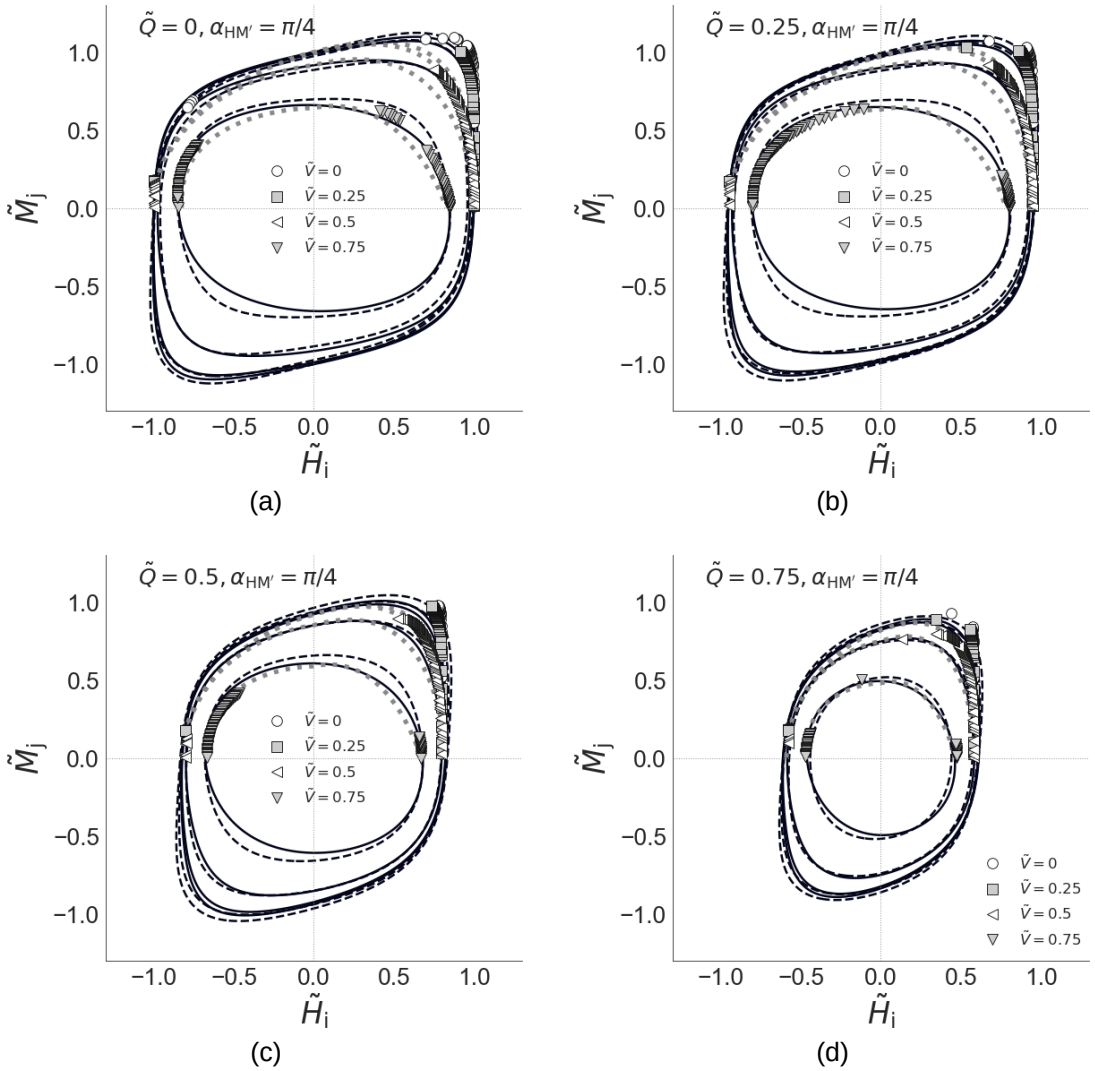

Figure 8. $\boldsymbol{HM}$ failure envelope contours for $\boldsymbol{\alpha_{HM'} = \frac{\pi}{4}, \tilde{V} = 0, 0.25, 0.5, 0.75}$ and (a) $\boldsymbol{\tilde{Q} = 0}$; (b) $\boldsymbol{\tilde{Q} = 0.25}$; (c) $\boldsymbol{\tilde{Q} = 0.5}$; (d) $\boldsymbol{\tilde{Q} = 0.75}$. The black dashed and solid lines are the contours represented by $\boldsymbol{f_4}$ and $\boldsymbol{f_6}$ respectively. The grey dotted lines are the contours represented by the Shen et al. (2017) formulation (i.e. Eq. 3).

4. Comparisons with previous failure envelope formulations

In this section, comparisons are made with HM contours determined from previous failure envelope formulations, which are typically calibrated using failure envelope data computed with a Tresca soil model. Such a comparison (noting that the current paper adopts a von Mises soil model) is considered valid for the following reasons: (i) although previous studies (e.g. Gourvenec et al. 2006) have indicated that the uniaxial capacities of the foundation are slightly

600 different for Tresca and von Mises soil, other studies (e.g. Gourvenec & Randolph 2003;
601 Gourvenec 2007) have shown that the HM contours of the failure envelopes for surface
602 foundations on Tresca and von Mises soil are similar in shape; (ii) in the following analysis, the
603 failure envelope data are normalised by their respective uniaxial capacities; the normalised HM
604 contours presented below (for von Mises soil) are therefore expected to be similar to
605 comparable studies employing Tresca soil.
606
607 Figs. 5 to 8 provide a comparison between HM contours determined from the previous 6DoF
608 failure envelope formulation by Shen et al. (2017) and the current approach. It can be observed
609 from these figures that a key advantage of f_4 and f_6 is that they are well-defined in all quadrants
610 of the HM load space, whereas the Shen et al. (2017) formulation (i.e. Eq. 3) is not real-valued
611 for negative M values due to the fractional exponent a in its formulation. Being well-defined in
612 the entire load space makes f_4 and f_6 highly suitable for macro-element modelling, as these
613 models accept both negative and positive load values as inputs. Furthermore, Fig. 7 shows that
614 only f_4 and f_6 are able to accurately capture the change in the HM contours of the failure
615 envelope as $\alpha_{HM'}$ varies, including symmetric HM contours when $\alpha_{HM'} = \pi/2$.
616
617 For planar VHM loading, Fig. 9 compares the HM contours represented by f_4, f_6 and the
618 previous formulations (as described in Section 1.2) with the 3D finite element data. The Vulpe et
619 al. (2014) and Shen et al. (2017) formulations are not real-valued for negative M values due to
620 the fractional exponents in their formulations. The formulation of Taiebat & Carter (2000) has
621 the advantage of being well defined in all quadrants of the load space, while the formulation of
622 Shen et al. (2017) has the closest match to the 3D finite element results out of the previous
623 formulations.
624
625 Fig. 10 compares the $VH,\ VM,\ QH$ and QM contours represented by f_4, f_6 and the previous
626 formulations with the 3D finite element data. It is evident that the formulations of Taiebat &
627 Carter (2000) and Shen et al. (2017) offer similar levels of agreement with the 3D finite element
628 data. However, Taiebat & Carter (2000) has the advantage of being well-defined in all quadrants

of the load space, while the formulation of Shen et al. (2017) is not real-valued for negative values of M, V and Q due to the fractional exponents in the formulation.

In general, it is evident from Figs. 5 to 10 that both f_4 and f_6 provide a close approximation to the 3D finite element failure loads.

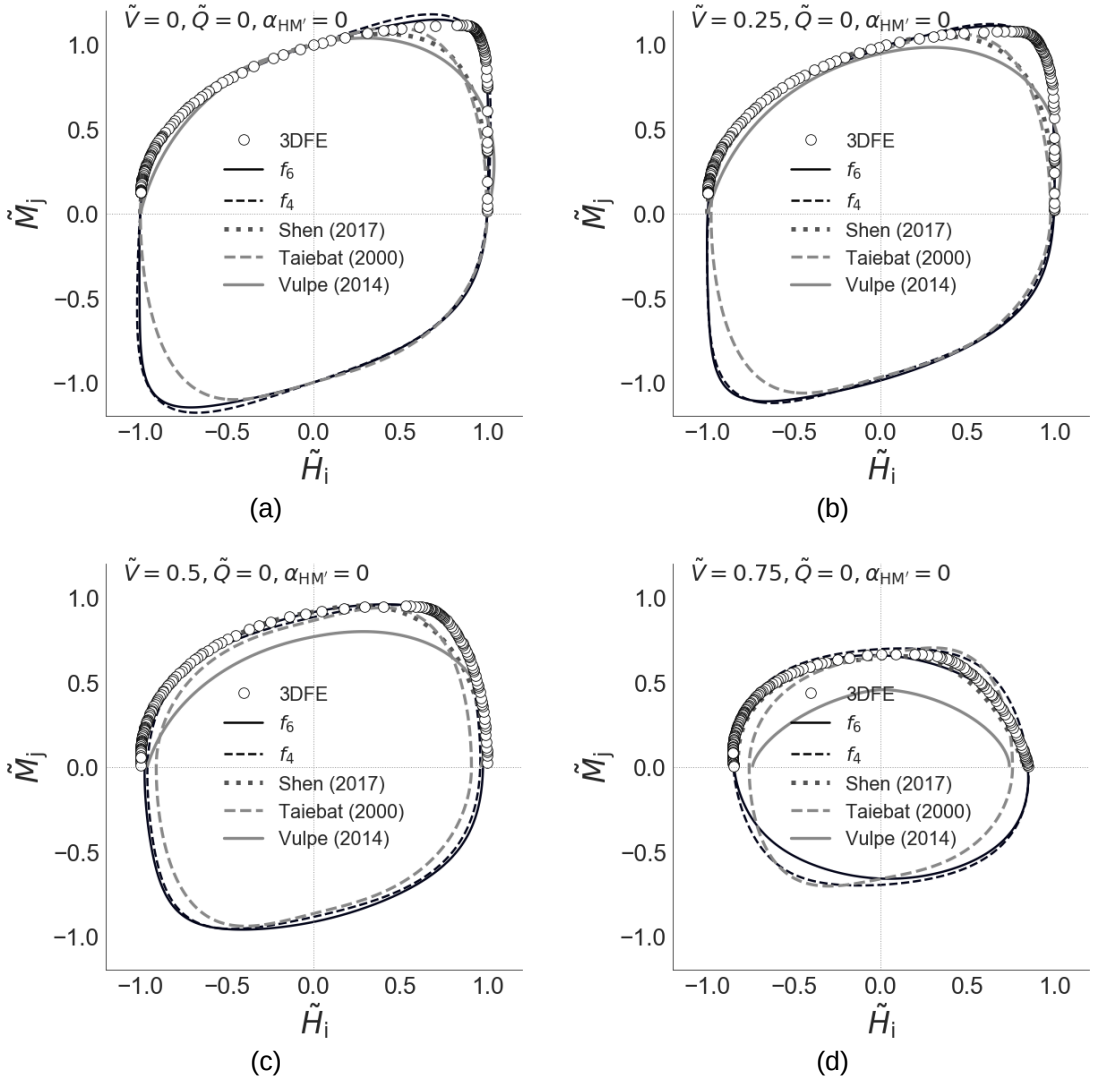

Figure 9. $\boldsymbol{HM}$ failure envelope contours for $\boldsymbol{\alpha_{HM'}=0}$, $\boldsymbol{\widetilde{Q}=0}$ and (a) $\boldsymbol{\widetilde{V}=0}$; (b) $\boldsymbol{\widetilde{V}=0.25}$; (c) $\boldsymbol{\widetilde{V}=0.5}$; (d) $\boldsymbol{\widetilde{V}=0.75}$.

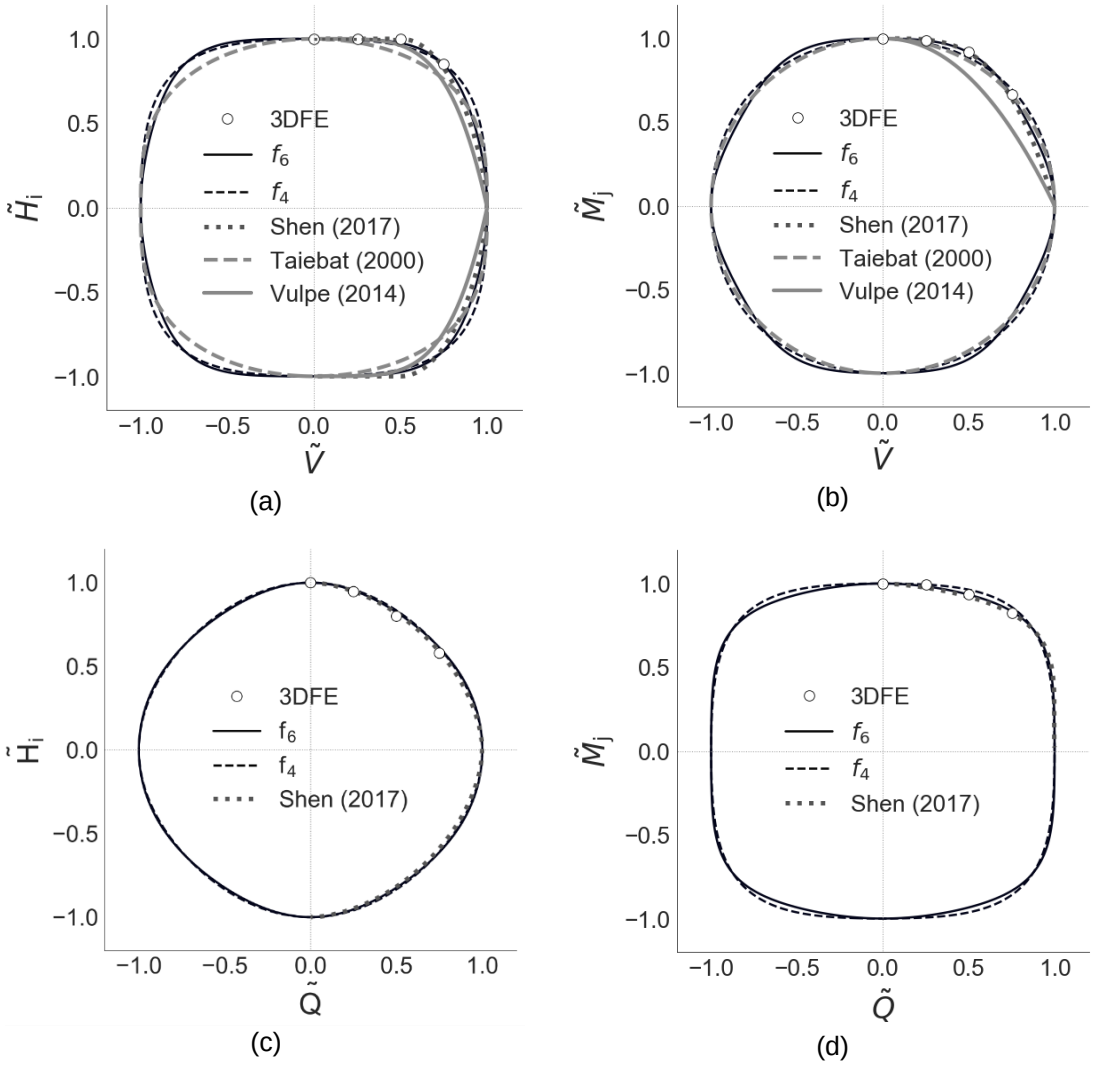

Figure 10. (a) $\boldsymbol{VH}$ (b) $\boldsymbol{VM}$ (c) $\boldsymbol{QH}$ and (d) $\boldsymbol{QM}$ failure envelope contours.

5. Macro-element model example

To demonstrate the application of the proposed convex failure envelope formulations in a macro-element model, f_4 was implemented as the yield surface and the plastic potential for an elastic perfectly-plastic macro-element model for a rigid, circular surface foundation on von Mises soil, with the elasto-plastic integration performed using the implicit closest point projection method (Simo & Hughes, 2006). The 4th degree formulation f_4 was selected for this demonstration, rather than f_6 , as it offers good accuracy while being relatively concise. The uniaxial capacities were obtained from the 3D finite elements results (as listed in Table 1) and

655 the elastic stiffness matrix for the macro element was determined from the elastic stiffness
656 formulations for a suction caisson foundation with zero skirt length (i.e. equivalent to a circular
657 surface foundation), as detailed in Suryasentana et al. (2020b).
658
659 Fig. 11 compares the macro-element calculations of the load-displacement behaviour with
660 corresponding 3D finite element results, for a sequential swipe test in the HM load space (see
661 Fig. 4) under non-planar HM loading ($\alpha_{S\Theta} = \pi/4$) with $\tilde{V} = 0.5$ and $\tilde{Q} = 0.25$. The macro-
662 element calculations agree well with the 3D finite element results, especially the variation of $\tilde{H}_x$
663 and $\tilde{H}_y$ during the sequential swipe test.
664
665 Fig. 12 shows the normalised H_x-M_x and H_y-M_x failure envelopes resulting from sequential
666 swipe test depicted in Fig. 11. It is clear that the macro-element model is able to reproduce the
667 3D finite element results very well, especially the changes in the $\tilde{H}_x$-$\tilde{M}_x$ and $\tilde{H}_y$-$\tilde{M}_x$ contours of
668 the failure envelope under non-planar HM loading. A key advantage of the macro-element
669 model is its efficiency relative to the 3D finite element model; it took 14 seconds to generate the
670 data points in Fig. 12, while the 3D finite element model took 1.7 hours.
671
672
673
674
675
676
677
678
679
680

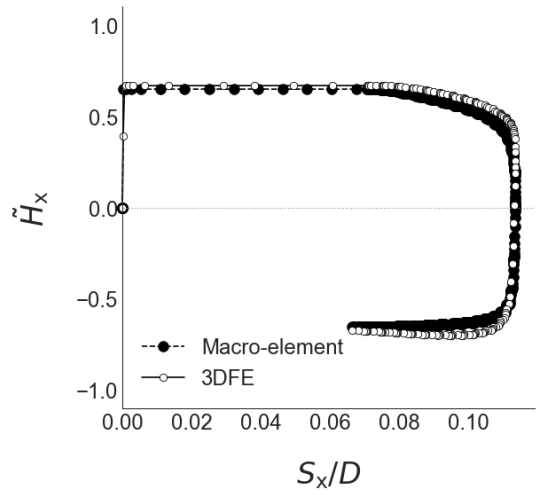

(a)

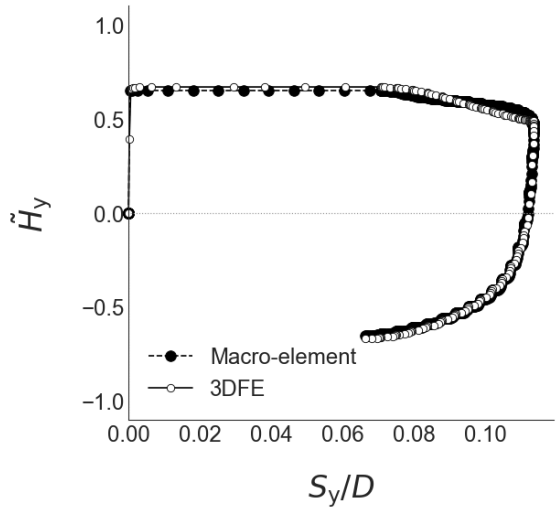

(b)

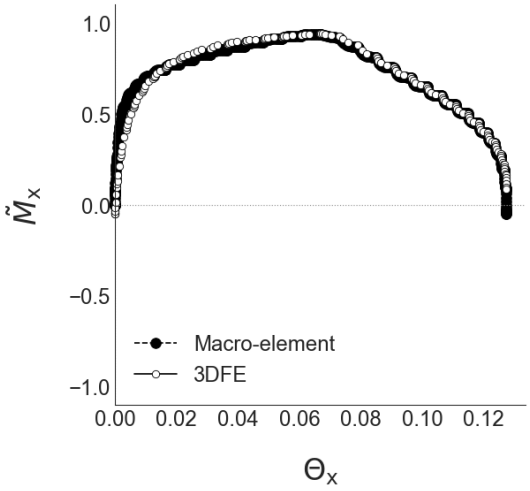

(c)

Figure 11. Comparison of the load-displacement behaviour – computed with the macro-element model and 3D finite element analysis - for a sequential swipe test in the HM load space for $\alpha_{s\Theta} = \frac{\pi}{4}, \tilde{V} = 0.5, \tilde{Q} = 0.25$.

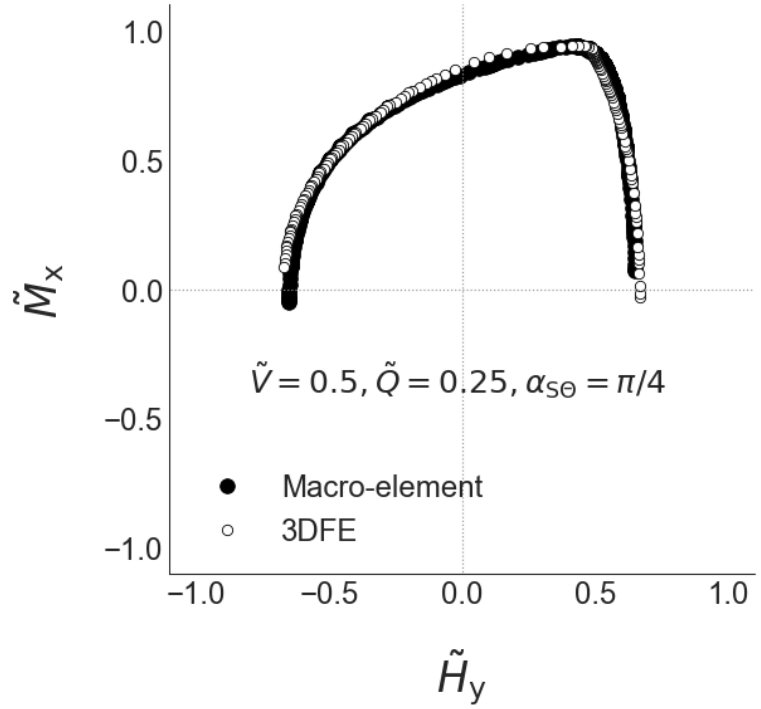

(a)

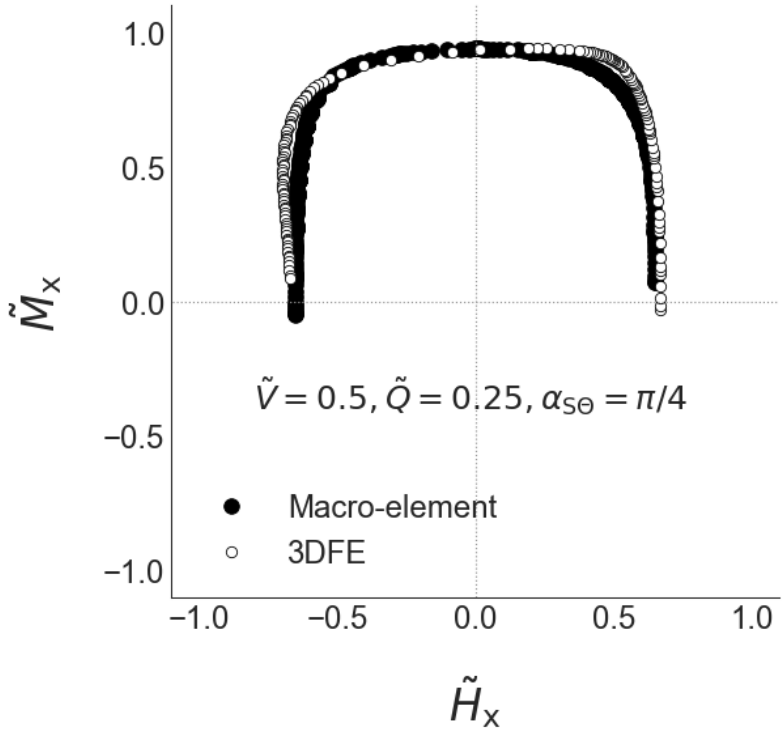

(b)

Figure 12. Normalised H_y-M_x and H_x-M_x failure envelopes computed in the sequential swipe test depicted in Fig. 11.

6. Discussion

Two failure envelope formulations, f_4 and f_6, have been derived for a rigid, circular surface foundation on undrained clay for 6DoF loading; they have been shown to provide a close match with 3D finite element calibration data. The optimisation process to determine the coefficients in f_4 and f_6 is reasonably fast, taking about 5 and 9 minutes respectively, using a computer with an Intel Core i7 1.90 GHz processor with 32 GB RAM (random access memory).

Although f_4 and f_6 may seem rather intimidating due to their relatively large number of terms, they are simple expressions that are easily differentiable, making them suitable for use as yield functions and plastic potentials in macro-element models. Other advantages include guarantees of global convexity and thermodynamics consistency (as explained in Suryasentana et al. 2020a).

Although the proposed procedure involves deriving the formulation in the reduced 5DoF load space before redefining it in 6DoF space, this is not a requirement of the method; the SOS-convex polynomial framework can derive a formulation in the full 6DoF load space directly, on the basis of the finite element failure load calibration data. The procedure outlined in the paper is, however, advantageous for the following principal reasons: (i) the reduced dimensionality of the 5DoF load space makes it easier and faster for the YALMIP toolbox to evaluate the polynomial coefficients, since the search space is reduced; (ii) a larger number of failure load calibration data would be needed to train the YALMIP toolbox to recognise the invariant property of the failure envelope with respect to horizontal and moment loading.

For cases where the ground model has spatial variations in the horizontal plane, the proposed ‘define in the reduced 5DoF load space before redefining it in 6DoF space’ approach is not applicable (since the failure envelope is no longer invariant to changes in the absolute directions of the resultant horizontal and moment loads). For these cases, the failure envelope formulation would need to be derived in the full 6DoF load space directly.

The proposed failure envelope formulations (Eqs. 23 and 24) are only applicable to undrained clay with uniform shear strength. However, the proposed procedure can be readily employed to determine failure envelope formulations for soils with non-uniform shear strength. The failure envelope analyses presented in the paper employ the assumption of no contact breaking at the soil-foundation interface. This approach is adopted to demonstrate the proposed convex failure envelope formulation procedure and to compare with previous independent work (Shen et al. 2017) in which this same interface condition was employed.

The no contact breaking assumption is applicable to offshore foundation cases where significant pore pressure suctions can develop beneath the footing. Alternatively, a zero-tension condition could be enforced at the soil-footing interface; in this case the failure envelope will differ from those presented in the current paper in several respects. The moment capacity, for example, will be reduced at low values of vertical loads compared to the no contact breaking case (e.g. Shen et al. 2016). Also, the current work assumes that the soil-footing interface is fully adhesive whereas a frictional soil-foundation interface might be more representative of real conditions. A frictional interface, for example, will tend to reduce the capacity in torsion, especially for low values of vertical load. The development of convex failure envelopes incorporating contact breaking and frictional interfaces is a topic for future work.

7. Conclusion

The paper describes an automated procedure for deriving failure envelope formulations for a circular surface foundation on undrained clay for 6DoF loading, a process that previously required significant manual interpretation. Besides the efficiency of the procedure, the derived failure envelope formulations offers advantages over existing formulations, such as (i) guaranteed global convexity; (ii) being well-defined in the entire load space (which allows the formulation to be used for both ultimate capacity evaluations and macro-element modelling), and (iii) accurate modelling of the failure envelope for non-planar horizontal and moment loading.

An example macro-element model is demonstrated, with one of the derived failure envelope formulations acting as the yield function and plastic potential of the model. The macro-element model is able to accurately reproduce the 3D finite element results with high efficiency.

Although this study has applied the procedure to derive a 6DoF failure envelope formulation for a circular surface foundation, the procedure is applicable for other circular foundation types. Thus, this main significance of this work is that it addresses one of the key barriers to the adoption of the failure envelope approach, as identified by previous researchers, which is the difficulty in deriving failure envelope formulations (especially in higher dimensional load space beyond VHM). This study should be regarded as the first step towards more site-specific failure envelope formulations and reducing the barriers to more widespread adoption of the failure envelope approach for ultimate capacity assessments or macro-element modelling in the 6DoF load space.

Acknowledgments

This work was completed during the DPhil studies of the first author and he would like to acknowledge the generous support of Ørsted Wind Power for funding his DPhil studentship at the University of Oxford. Byrne is supported by the Royal Academy of Engineering under the Research Chairs and Senior Research Fellowships scheme.

References

API (2011). Recommended practice 2GEO geotechnical and foundation design considerations. Washington (DC, USA): American Petroleum Institute.

Bienen, B., Byrne, B. W., Houlsby, G. T. & Cassidy, M. J. (2006), 'Investigating six-degree-of freedom loading of shallow foundations on sand', Géotechnique 56(6), 367–379.

Butterfield, R., Houlsby, G. T. & Gottardi, G. (1997), 'Standardized sign conventions and notation for generally loaded foundations', Géotechnique 47(5), 1051–1054.

784 Chen, W. F. & Liu, X. L. (1990), Limit analysis and soil plasticity, Elsevier Ltd., Amsterdam.
785 Dassault Systèmes (2014), Abaqus user manual, Simula Corp., Providence, RI.
786 Finnie, I. M. S. & Morgan, N. (2004). Torsional loading of subsea structures. In The Fourteenth
787 International Offshore and Polar Engineering Conference. International Society of Offshore
788 and Polar Engineers.
789 Feng, X., Randolph, M. F., Gourvenec, S. & Wallerand, R. (2014a), Design approach for
790 rectangular mudmats under fully three-dimensional loading. Géotechnique 64(1), 51–63.
791 Feng, X., Gourvenec, S., & Randolph, M. F. (2014b). Optimal skirt spacing for subsea mudmats
792 under loading in six degrees of freedom. Applied Ocean Research, 48, 10-20.
793 Feng, X., & Gourvenec, S. (2015a). Consolidated undrained load-carrying capacity of subsea
794 mudmats under combined loading in six degrees of freedom. Géotechnique, 65(7), 563-575.
795 Feng, X., Gourvenec, S., Randolph, M. F., Wallerand, R., & Dimmock, P. (2015b). Effect of a
796 surficial crust on mudmat capacity under fully three-dimensional loading. Géotechnique, 65(7),
797 590-603.
798 Gourvenec, S. (2007). Failure envelopes for offshore shallow foundations under general loading.
799 Géotechnique, 57(9), 715-728.
800 Gourvenec, S., & Randolph, M. (2003). Effect of strength non-homogeneity on the shape of failure
801 envelopes for combined loading of strip and circular foundations on clay. Géotechnique, 53(6),
802 575-586.
803 Gourvenec, S., Randolph, M., & Kingsnorth, O. (2006). Undrained bearing capacity of square and
804 rectangular footings. International Journal of Geomechanics, 6(3), 147-157.
805 ISO (2016). ISO 19901-4: Petroleum and natural gas industries specific requirements for offshore
806 structures – part 4: geotechnical and foundation design considerations, 2nd edn. Geneva,
807 Switzerland: International Standards Organisation.
808 Löfberg, J. (2004), YALMIP : a toolbox for modeling and optimization in MATLAB, in '2004 IEEE
809 International Conference on Robotics and Automation', IEEE, pp. 284–289.
810 Löfberg, J. (2009), 'Pre- and post-processing sum-of-squares programs in practice', IEEE
811 Transactions on Automatic Control 54(5), 1007–1011.
812 Martin, C. M. (1994). Physical and Numerical Modelling of Offshore Foundations Under
813 Combined Loads. Ph.D. thesis, University of Oxford.

814 Paikowsky, S. G. (2010). LRFD design and construction of shallow foundations for highway bridge
815 structures (Vol. 651). Transportation Research Board.
816 Panteghini, A., & Lagioia, R. (2014). A fully convex reformulation of the original Matsuoka–Nakai
817 failure criterion and its implicit numerically efficient integration algorithm. *International Journal*
818 *for Numerical and Analytical Methods in Geomechanics*, *38*(6), 593-614.
819 Panteghini, A., & Lagioia, R. (2018a). An approach for providing quasi-convexity to yield functions
820 and a generalized implicit integration scheme for isotropic constitutive models based on 2
821 unknowns. *International Journal for Numerical and Analytical Methods in*
822 *Geomechanics*, *42*(6), 829-855.
823 Panteghini, A., & Lagioia, R. (2018b). An extended modified Cam-Clay yield surface for arbitrary
824 meridional and deviatoric shapes retaining full convexity and double
825 homothety. *Géotechnique*, *68*(7), 590-601.
826 Parrilo, P. A. (2003), 'Semidefinite programming relaxations for semialgebraic problems',
827 Mathematical Programming 96(2), 293–320.
828 Salciarini, D., & Tamagnini, C. (2009). A hypoplastic macroelement model for shallow foundations
829 under monotonic and cyclic loads. Acta Geotechnica, 4(3), 163-176.
830 Shen, Z., Feng, X., & Gourvenec, S. (2016). Undrained capacity of surface foundations with zero-
831 tension interface under planar VHM loading. Computers and Geotechnics, 73, 47-57.
832 Shen, Z., Bie, S. & Guo, L. (2017). Undrained capacity of a surface circular foundation under
833 fully three-dimensional loading. Computers and Geotechnics 92, 57–67.
834 Simo, J. C. & Hughes, T. J. (2006). Computational inelasticity (vol. 7). New York, NY, USA:
835 Springer Science & Business Media.
836 Suryasentana, S. K., Burd, H. J., Byrne, B. W., & Shonberg, A. (2020a). A systematic framework
837 for formulating convex failure envelopes in multiple loading dimensions. Géotechnique, 70(4),
838 343-353.
839 Suryasentana, S. K., Burd, H. J., Byrne, B. W., & Shonberg, A. (2020b). A Winkler model for
840 suction caisson foundations in homogeneous and non-homogeneous linear elastic soil.
841 Géotechnique (ahead of print). doi:10.1680/jgeot.19.p.172.

842 Suryasentana, S. K., Dunne, H. P., Martin, C. M., Burd, H. J., Byrne, B. W., & Shonberg, A.
843 (2020c). Assessment of numerical procedures for determining shallow foundation failure
844 envelopes. Géotechnique, 70(1), 60-70.
845 Taiebat, H. A. & Carter, J. P. (2000). Numerical studies of the bearing capacity of shallow
846 foundations on cohesive soil subjected to combined loading. Géotechnique 50, No. 4,
847 409–418.
848 Tan, F. (1990). Centrifuge and theoretical modelling of conical footings on sand. Ph.D. thesis,
849 University of Cambridge.
850 Vulpe, C., Gourvenec, S. & Power, M. (2014). A generalised failure envelope for undrained
851 capacity of circular shallow foundations under general loading. Géotechnique Letters 4,
852 No. 3, 187–196.